



Studying key processes related to CO₂ underground storage at the pore scale using hihg pressure micromodels

Sandy Morais, Anaïs Cario, Na Liu, Dominique Bernard, Carole Lecoutre,
Yves Garrabos, Anthony Ranchou-Peyruse, Sébastien Dupraz, Ryan L.
Hartman, Samuel Marre

► To cite this version:

Sandy Morais, Anaïs Cario, Na Liu, Dominique Bernard, Carole Lecoutre, et al.. Studying key processes related to CO₂ underground storage at the pore scale using hihg pressure micromodels. *Reaction Chemistry & Engineering*, Royal Society of Chemistry, 2020, 5 (7), pp.1156-1185. 10.1039/D0RE00023J . hal-02641414

HAL Id: hal-02641414

<https://hal.archives-ouvertes.fr/hal-02641414>

Submitted on 3 Jul 2020

HAL is a multi-disciplinary open access archive for the deposit and dissemination of scientific research documents, whether they are published or not. The documents may come from teaching and research institutions in France or abroad, or from public or private research centers.

L'archive ouverte pluridisciplinaire **HAL**, est destinée au dépôt et à la diffusion de documents scientifiques de niveau recherche, publiés ou non, émanant des établissements d'enseignement et de recherche français ou étrangers, des laboratoires publics ou privés.



Studying key processes related to CO₂ underground storage at the pore scale using high pressure micromodels

Received 00th January 20xx,
Accepted 00th January 20xx

DOI: 10.1039/x0xx00000x

www.rsc.org/

Sandy Morais,^a Anaïs Cario,^a Na Liu,^a Dominique Bernard,^a Carole Lecoutre^a, Yves Garrabos^a, Anthony Ranchou-Peyrusse,^b Sébastien Dupraz,^c Mohamed Azaroual,^c Ryan L. Hartman,^d and Samuel Marre^{*a}

In this review, we present a general overview of the current progress in pore scale experimentations related to CO₂ geological storage. In such processes occurring in porous media, most of the phenomena start from (bio)geochemical reactions and transport mechanisms at the pore scale. Therefore, in order to predict the overall consequences of CO₂ injection inside a deep reservoir and to ensure a safe installation, it is essential to access pore-scale information for geochemical numerical methods and to improve the understanding of the critical operating parameters. In this view, high pressure micromodels that mimic geological media (Geological Labs on Chip) have recently attracted interest to study multiphase flows and chemical reactivity in porous media. Emphasis is placed on experiments that can be performed in realistic pressure conditions representative of deep geological formations, for accessing information on reactive flows in porous media, mineralization/dissolution, but also (bio)chemical processes. The use of such micromodels continues to broaden the investigation space thanks to the design of *in situ* characterization techniques. Together high-fidelity data not easily accessed in conventional batch or core-scale procedures is made readily available.

Introduction

The carbon dioxide atmospheric level is considered the main contribution to global warming, which is mostly caused by anthropogenic production from the overuse of fossil fuels (~36.2 Gt/year in 2017^{1,2}). The management of anthropogenic CO₂ will be one of the main challenges of this century. It is now critical, not only to develop technologies allowing the reduction of CO₂ emissions, but also to provide solutions to capture and use/store industrial CO₂ emissions. In this context, CO₂ Geological Storage (CGS) strategies have been largely considered and studied. These strategies include storing large quantities of CO₂ within: (1) unmined coal beds,³ (2) depleted oil and gas reservoirs,⁴ and (3) deep saline aquifers, which exhibit by far the widest estimated storage capacity (estimated storage capacity over ten trillion tons of CO₂)⁵. CGS could potentially contribute to the storage of ~15 Gt/year of CO₂ by 2050, representing roughly a third of the annual anthropogenic CO₂ emissions.⁶

The first two CGS strategies have been the most attractive ones, since they exhibit direct economic benefits when combined

with methane and oil production (Enhanced Oil recovery – EOR).⁷ Therefore, most of the studies dealing with CO₂ storage have been focused on these options over the last twenty years, leading to great advancement of the scientific knowledge. On the other hand, CO₂ storage in aquifers has been considered costly insofar as no direct profits can be made. Among targeted sites, deep aquifers generally consist of a layer of permeable rock filled with brackish waters (salinity ranging from 25 to 225 g.L⁻¹)⁸ and capped with a non-porous rock (caprock), providing a safer barrier than other candidates for geological reservoirs. Besides, whereas oil reservoirs or coal beds are unequally distributed around the world, deep aquifers can be found almost everywhere and represent ~2% of the total water volume of the oceans.⁹ This results in the largest estimated capacity for CO₂ storage (between 10 and 100 Tt),¹⁰ making aquifers the best possible CO₂ storage locations for long term anthropogenic CO₂ mitigation.

The geological carbon sequestration in aquifers has been studied and performed in several storage locations around the world, determining its technical feasibility as well as economic viability.¹¹ Where the prospective storage sites, it is now critical to adapt science and available technology (mainly provided by the oil industry), to enable operators to develop storage technologies and ensure their safe deployment around the world. The related R&D activities are based on geosciences, physics, chemistry, hydrodynamics, microbiology, etc. in order to achieve integrated responses and to unlock scientific and

^a CNRS, Univ. Bordeaux, Bordeaux INP, ICMCB, F-33600, Pessac cedex, France.

^b EEM-IPREM, UPPA, Technopôle Helioparc, 2 avenue P. Angot, 64053 Pau Cedex 9, France.

^c BRGM, 3 avenue Claude-Guillemen, BP 36009, 45060 Orléans Cedex 2, France.

^d Department of Chemical and Biomolecular Engineering, New York University, 6 MetroTech Center, Brooklyn, NY 11201, USA.

† Footnotes relating to the title and/or authors should appear here.

Electronic Supplementary Information (ESI) available: [details of any supplementary information available should be included here]. See DOI: 10.1039/x0xx00000x

technological issues upon which the success of industrial operations is conditioned.

These requirements mostly depend on the understanding of phenomena involved during the underground CO₂ injection. Indeed, when CO₂ is injected into a geological formation, it can undergo several trapping mechanisms, namely: (i) the stratigraphic trapping, (ii) the residual trapping, (iii) the solubility trapping and (iv) the mineral trapping.^{12, 13}

The stratigraphic trapping is the first mechanism occurring in the CO₂ geological storage process in aquifers. Once injected, the CO₂ percolates up through the porous rocks and towards the surface due to its lower density compared to the brine. It is then stuck below a caprock (shale or salt beds) of low permeability, preventing the propagation of ascending CO₂ plumes, stopping both upward flows and lateral escape.¹⁴ The residual trapping occurs on short time scales and is driven by capillary effects, correlated to the local interfacial tension, contact angle and pore sizes. During the CO₂ migration through the porous rocks, the CO₂ plume, followed by brine in a spontaneous imbibition process, leaves behind some isolated and immobilized blobs. Hence, CO₂ that is stored by this residual fluid trapping will stay in the storage site for long periods of time.¹⁵ These residual trapped CO₂ bubbles will gradually dissolve into the brine already present forming carbonates (CO₃²⁻) and hydrogencarbonate (HCO₃⁻) anions, and this mechanism greatly decreases the risk of leakage.¹⁶ This dissolution step constitutes the solubility trapping. The solubility of CO₂ varies as a function of pressure, temperature, and salinity/composition of the surrounding brine.¹⁷⁻¹⁹ The final trapping mechanism (mineral trapping) occurs when the cations released by the mineral dissolution of the rocks (due to the acidification of the brine) react with the dissolved carbonate species to form stable carbonate minerals. Most of these geochemical reactions take place slowly within a time frame of decades to centuries and their precipitation rate depends on the rock type (both the initial substrate and the precipitated minerals) and brine composition, the temperature, the partial pressure of CO₂ but also somewhat on the total pressure. Nevertheless, this trapping mechanism represents the ultimate step and the most secure form of CO₂ storage.^{20, 21}

These trapping mechanisms have been mostly studied at field and core scales (both numerically and experimentally). However, these strategies lack the pore scale view (1-100 μm), at which most of the processes occurs, such as mass transfer, surface reactivity, biofilms formation etc. In order to address these limitations, micromodels (on chip porous media) were developed and used to study multiphase flow and chemical reactivity in porous media. One of the earliest 2D micromodels was developed by Lenormand *et al.* in the eighties.^{22, 23} It was a random square network patterned in resin and was used to investigate the micro-scale mechanisms involved in the water displacement of oil in porous media. Since then, micromodels have been extensively developed, mostly thanks to the development of microfluidics and microfabrication techniques. For the particular case of carbon geological sequestration applications, the current trend concerns the designs of micromodels mimicking closely real, native porous media

(porosity and permeability heterogeneities, surface wettability and reactivity, etc.). Thus, these micromodels extract some geometrical information from real porous structure and include some essential schematization of reality.

Some of the main limitations so far were the actual pressure and temperature conditions, which can be used in these micromodels. In most cases, the carbon dioxide is injected into the reservoir at supercritical conditions. This is explained by the p,T conditions of the majority of the already used and targeted storage geological reservoirs, which overcome the CO₂ critical point (P_c = 73.9 bar, T_c = 31.0 °C). Hence, the injection benefits from the very advantageous properties of supercritical fluids. Indeed, beyond these p,T conditions, the CO₂ is dense with a low viscosity. This gives the possibility of storing a large amount of CO₂ in a reduced volume and ease its invasion into the brine-filled porous reservoir. Additionally, supercritical CO₂ generally has a higher solubility in aqueous phases than its gas or liquid state. Therefore, the ability to access experimental data at pore scale for CO₂ supercritical conditions constitutes a fundamental need.

Nevertheless, most of the studies considered ambient conditions, which are not representative of real reservoir conditions, although critical information on the involved pore scale mechanisms could be obtained.²⁴ These limitations primarily result from the materials considered for the micromodels fabrication such as glass or polymers (PMMA, PDMS), along with the interfacing technologies, which do not provide enough mechanical strength for reaching such harsh conditions (typically pressures range between 6 MPa and 15 MPa and temperatures between 30°C and 80°C). To overcome these limitations, silicon-Pyrex micromodels have been developed based on the recent rise of high-pressure microfluidics approaches, which has been previously applied to various fields of research.^{25, 26} Such systems open avenues to investigate and to display pore scale physical and chemical processes in porous media at aquifer conditions. Besides their mechanical strength, they provide good thermal resistance and chemical inertness, while maintaining an optical access through the Pyrex side.

In this review, we present, through selected examples, the recent developments in micromodels for investigating CO₂ geological storage at the pore scale (Geological Labs on Chips, GLoCs), starting with current strategies for designing and characterizing micromodels. Next, we address the use of the GLoCs for accessing key parameters involved in CO₂ geological storage, from a geo(bio)chemistry, an engineering, and physics points of view. Finally, we discuss some current challenges and opportunities for these microscale tools to investigate at the pore scale other deep underground relative topics (CO₂ conversion, hydrogen storage, geothermal energy, Enhanced Oil Recovery, etc.).

1. Pore scale view of phenomena

Over the last few years, many studies have been conducted to understand two-phase flow in porous media with different

fluids. A large part of the literature has investigated drainage and imbibition processes. The first consists of a non-wetting fluid displacing a wetting fluid, while the second is the process involved when a wetting fluid displaces a non-wetting fluid.²⁷ A large number of factors influences the flow processes in a porous medium, in particular at the pore scale, such as the fluid's viscosity and density, the porosity and permeability, the interfacial tension, the wetting properties, the heterogeneity of the porous media or the fluid injection flowrates.

The porous medium is characterized by its porosity ϕ , defined by the ratio between the volume of the pores (V_p) and the total volume (V_t):²⁸

$$\phi = \frac{V_p}{V_t} \quad (1)$$

During drainage or imbibition processes, two parameters can be distinguished. First, the saturation S which is the fraction of the pores filled with a fluid phase, meaning the ratio between the volume of the pores filled with the fluid and the total pore volume: $S = V_f / V_p$. Then, the absolute permeability K (m^2 or Darcy) is the resistance of the porous medium towards flow of a fluid in its pores.

In the case of a monophasic flow of a non-compressible Newtonian fluid, the permeability is linked by the Darcy Law to the dynamic viscosity of this fluid, μ (Pa·s):²⁹

$$\vec{u} = -\frac{K}{\mu} \vec{\nabla} P \quad (2)$$

Note that this equation neglected the gravitational effects as it is used for a microfluidic application. Also, it considers the deformation of the porous media negligible and that the flow in the pores respects the Stokes equation. Under its vector form, the permeability is also linked to the pressure gradient and the Darcy velocity u ($m.s^{-1}$, $\vec{u} = \vec{Q} / A$, where Q is the flow rate and A the specific area of the porous medium). Note also that for a homogeneous porous media bearing some anisotropies, the permeability need to be a tensor.

In two-phase flow, it is necessary to deal with pore scale interactions and particularly the wetting and the capillarity effects between the two phases. The wettability of the porous media skeleton is a critical factor to understand the capillary pressure. This consists in studying of the ability of a fluid to maintain contact with a solid surface. This results from the competition between the adhesive interactions of the fluid and the cohesive forces between the fluid molecules. In the case of the injection of CO_2 into the aquifer filled with brine, the aqueous brine is typically the wetting phase and the injected CO_2 is usually considered as the non-wetting phase.

Another key parameter to predict fluid distribution and behavior in the porous medium is the capillary pressure. In other words, how the CO_2 phases are trapped by capillary forces. These forces prevent the invading fluid from a spontaneous entering in the porous medium. To enter a pore throat (of radius r_1 and r_2), its pressure has to exceed the pressure of the displaced phase by a value P_c , capillary pressure, given by the Young-Laplace equation where γ is the interfacial tension between the two fluid phases:³⁰

$$P_c = \gamma \left(\frac{1}{r_1} + \frac{1}{r_2} \right) \quad (3)$$

In the case where the invasion process is only governed by capillary forces, the pressures of the different phases are uniform and the front separating the two fluids penetrates first the largest pore throat, where the capillary resistance is the smallest.³¹ But in the presence of both viscous and capillary forces the pressures are not uniform anymore. The viscous forces will modify the difference of pressure between the two fluids and promote the entrance of the invading fluid in smaller throat. In this case, two dimensionless parameters will characterize the interface displacements. Firstly, the capillary number Ca , given by the equation:

$$Ca = \frac{\mu u}{\sigma} \quad (4)$$

where μ and u are the dynamic viscosity (Pa·s) and the Darcy velocity ($m.s^{-1}$) of the penetrating fluid, respectively. This number describes the relative importance of viscous forces to capillary forces. For example, for a low capillary number ($Ca < 10^{-5}$), capillary forces dominate the interface displacement, whereas for a high capillary number the viscous forces dominate the flow.

Although the viscous effects are negligible at macroscale, at the pore scale, the viscous ratio determines the stability of displacements. To specify the displacements of the interface during the drainage or imbibition process, a ratio between the absolute viscosity for each fluid is used, expressed as:

$$M = \frac{\mu_i}{\mu_d} \quad (5)$$

where μ_i is the absolute viscosity of the injected phase and μ_d the one of the displaced phase. For $M > 1$, the displacement is favorable whereas for $M < 1$ the displacement becomes unstable. In the listed studies at pore scale concerning CO_2 invasion in a saturated brine-filled reservoir, the unfavorable ratio M between CO_2 (regardless of p,T conditions) and the aqueous phase tends to lead to an instable displacement.

To account for both parameters, the early work of Lenormand *et al.* have proposed to classify the displacement mechanisms of two-phase flow in porous media in a $[Ca, M]$ phase diagram. Such diagrams have been helpful in the oil industry to optimize the injection parameters in order to maximize oil production.^{32, 33}

Besides hydrodynamics, most of the biological and geochemical processes occur at the pore scale where strong gradients arise leading to reactive fronts (bio)chemical reactions, which can be either thermodynamically or kinetically limited depending on the multiphase flow hydrodynamics, interfacial mass exchanges and the pore geometry. Considering the geochemistry existing during a CGS process, reactive flows evolve continuously through dissolution and precipitation phenomena in these three-phase systems (brine, CO_2 , rock minerals). Similarly, geobiological effects have to be taken into

Table 1 Examples of various micromodels reported in the literature.

Reference	Materials	Length (mm)	Width (mm)	Diameter cylindrical posts (μm)	Pore bodies (μm)	Pore throats (μm)	Porosity (ϕ)	Depth (μm)	Absolute permeability
Baumann et al. (2004) [42]	Silicon / Borosilicate Glass	-	-	300	173	35	0.38	50	-
Boyd et al. (2014) [43]	Silicon / Borosilicate Glass	20	10	300	180	40	0.39	35	-
Buchgraber et al. (2012) [44]	Silicon / Borosilicate Glass	-	-	50 to 300 (grains)	-	-	0.46	25	950 mD
Kazemifar et al. (2015) [45]	Silicon / Borosilicate Glass	12.5	12.5	400/200	300/100	100/300	0.51	30	-
Morais et al. (2016) [46]	Silicon / Borosilicate Glass	20	5	235/229	279/287	62/67	0.44/0.47	22.3/17.5	-
Zuo et al. (2013) [47]	Silicon / Borosilicate Glass	-	-	-	-	-	0.35	35	530 mD
Harrison et al. (2017) [48]	Silica	50	15	180 and 70		215 and 260	0.87	130	-
Kim et al. (2012) [49]	Silica	20	10	590	127 to 140	30 to 50		20 to 40	-
Miri et al. (2015) [50]	Glass	10	2	500 (square)	500	250	-	350	-
Zhang et al. (2011) [51] Wang et al. (2013) [52]	Glass	12.2	12.1	200/100	120/60	26.7/13.3	0.40	35	-

account since the microorganisms inhabiting deep underground can form biofilms and catalyze redox reactions (involving electron transfers between electron donors and electron acceptors). Such structures can modify locally not only the permeability and the porosity of the porous structures but also the local chemistry, being able to interact with both minerals surfaces and flowing fluid phases.

All these coupled mechanisms take place at the pore scale where the microscale dimensions of the flow result in small Péclet (P_e) numbers, representing the convection to diffusion effects:

$$P_e = \frac{2r u}{D} \quad (6)$$

where r is the pore radius and D is the diffusion coefficient of a molecule in the aqueous medium. As a result, mass transfer in pores is mostly diffusion-driven.

To determine the influence of reactive transport in complex geometries such as porous media to the (bio)chemical reactions kinetics, it is therefore interesting to introduce the dimensionless Damköhler number for flow and reaction³⁴, largely employed in chemical engineering for catalytic reactions, defined as:

$$D_a = \frac{k C_A^{n-1} (2r)^2}{D} \quad (7)$$

where C_A is the concentration of the specie "A", k and n are the kinetic constant and the order of the considered reaction. The D_a relates the chemical reaction rate (calculated from conventional rate laws) to the transport rate (convection or diffusion) occurring for a heterogeneous reaction. Therefore, when dealing with reactive flow in porous media, a high value of D_a , corresponds to large dissolution or precipitation rates or low flowrates, while a small value of D_a results from low reaction rates or high flowrates (low residence time). Both the P_e and the D_a numbers are therefore useful to predict and to characterize reactive transports in porous media, including local concentration gradients and the shape of the reactive fronts in multiphasic geo(bio)chemical reactions.³⁵⁻³⁸

All these parameters drive several important local phenomena in porous media such as the adsorption (selective or not) of molecules and microorganisms. Additionally, the formation of biofilms in rock pores can locally generate highly reactive micro-environments. Such effects greatly contribute to the surface passivation / activation of mineral substrates, which controls the reactive flow behavior. In this context, a pore scale investigation of the involved phenomena is highly desirable to establish models, which will be used to predict the overall behavior of a reservoir at larger scale under CGS conditions.

2. Strategies for designing adapted micromodels

As mentioned above, CGS requires knowledge at the pore scale, which can be obtained thanks to the use high pressure microfluidic porous media (micromodels or geological labs on a chip). Most of the reported studies concern the use of these approaches for determining:

- (i) The fluids repartitioned in the aquifer, including interfacial and capillary phenomena and fluid trapping mechanisms.
- (ii) The fluid's flows and their evolution during time and the impacts of flow regimes on the transport of CO_2 and eventual preferential flows.
- (iii) The geochemical processes, their location and kinetics (dissolution and precipitation reactions), the impact of the different solubility of gas mixtures on the local hydrodynamic properties of the reservoir rock
- (iv) The biological activity as the evolution of the microbial communities and their metabolisms.

All these experimental data can later be used to validate / optimize the numerous numerical modelling approaches from pore-scale to the reservoir scale.³⁹ Hence, geological micromodels can demonstrate to the CGS community the macroscale consequences of pore scale processes. Although field simulation would not be driven from pore-scale data, such experimental data can lead to a better accuracy of meso-scale

models and thus be crucial for the understanding of CGS or EOR technologies, particularly in terms of CO₂ injection safety and/or oil recovery.

Therefore, depending on the targeted data and processes to study, several strategies can be developed to fabricate and to design adapted micromodels, whether we are interested in pure fluid hydrodynamics, dissolution studies or reactive flows, which are detailed in this section.

2.1 Materials for micromodels fabrication

To investigate at the pore-scale the physical, chemical and biological processes associated with CO₂ geological storage technologies, micromodels primarily need to provide an optical access and a good HP/HT capability in order to be representative of the reservoir conditions but also to be complementary to core-scale approaches and to address the limitation of these conventional experimental set-ups. These micromodels investigations can take advantages of the recent developments of microfluidic conception, in terms of materials and fabrication process. In the past few years, the microsystems developed for this field of research consisted in 2D pore networks etched or molded into materials such as polymers (PDMS, PMMA), glass or silicon. While polymers micromodels (including PDMS - PolyDiMethylSiloxane or PMMA - PolyMethylMethAcrylate) are cheap and easy to make, they generally fail in accessing realistic *p*, *T* conditions – also new developments have been recently made⁴⁰ – and can present some limitations in terms of fluid compatibility (*e.g.* water pervaporation through PDMS).⁴¹ For realistic high pressure experimentations, the materials used for the micromodels fabrication are summarized in **Table 1**.^{42–52} The choice depends on the targeted study and the considered operating conditions (**Fig. 1**)^{24, 44, 46, 47, 49, 51–58}.

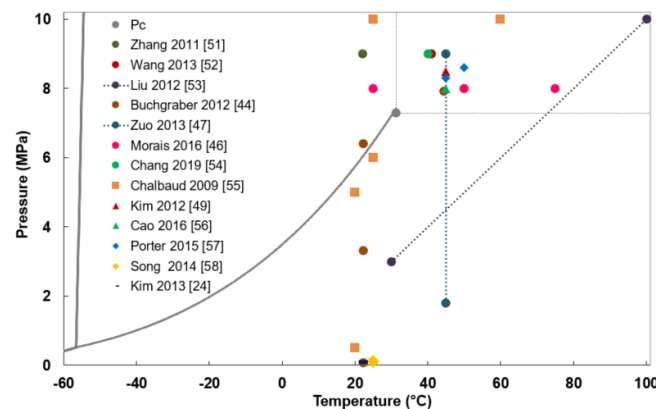


Fig. 1 CO₂ phase diagram and p-T conditions reported for the CO₂ storage pore scale studies using micromodels approaches along with the associated microsystem materials. Si/Pyrex microsystems (●), Glass/Glass microsystems (■), fused silica microsystems (▲), geological materials microsystems (◆), PDMS microsystems (—).

Glass/glass micromodels display better properties concerning the pressure resistance and the chemical inertness but can be limited when temperature gradient is applied on micromodels.^{59, 60} The Si/Pyrex chips, as the glass ones, certainly need tough fabrication

conditions (clean room) and can be expensive but outperform the others in pressure and temperature resistance.²⁵

2.2 Design geometries

In view of an incremental type of research, the first interest of using micromodels has been focused on visualizing and studying multiphase flows in porous media, without integrating any geo(bio)chemistry or fluid / surface reactions, but rather focusing on hydrodynamics. In this context, two types of geometries have been typically considered: simplified and realistic.

Basic design micromodels. Simple designed porous media geometries primarily aim to provide researchers general trends in thermo-hydrodynamical behavior of multi-phase flows in porous-like systems. They are purposefully kept “simple” to: (i) minimize the complexity of real pore geometry for reactive and non-reactive flows and (ii) facilitate the microfabrication process and the characterization. They generally consist in cylindrical plots or squares following a square or staggered arrangement more or less homogeneous (**Fig. 2**).^{42, 43, 46, 49}

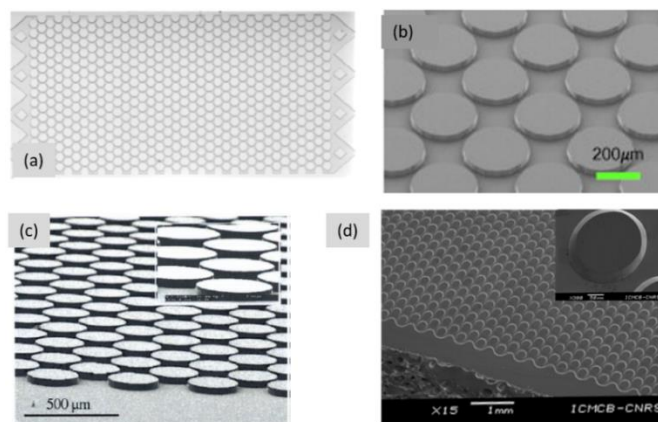


Fig. 2 Examples of simplified geometries: (a) Photograph of a micromodel for dewetting studies⁴⁹, adapted) with permission from Kim Y., Wan J., Kneafsey T.J., Tokunaga T.K. Dewetting of silica surfaces upon reactions with supercritical CO₂ and brine: pore-scale studies in micromodels. *Environmental Science and Technology* 2012, vol. 46, p. 4228–4235. Copyright (2020) American Chemical Society. (b) scanning electron microscope image of pore structure in the micromodel containing a staggered array of evenly spaced cylindrical posts⁴³, adapted with permission from Boyd V., Yoon H., Zhang C., Oostrom M., Hess N., Fouke B., Valocchi A. J., Werth C. J. Influence of Mg²⁺ on CaCO₃ precipitation during subsurface reactive transport in a homogeneous silicon-etched pore network. *Geochimica et Cosmica Acta* 2014, vol. 135, p. 321–335. Copyright (2020) Elsevier. (c) scanning electron microscope image of a homogeneous micromodel used for μPIV experiments⁴², adapted with permission from Baumann T., Werth C. J. Visualization and modeling of polystyrol colloid transport in a silicon micromodel. *Vadose Zone Journal* 2004, vol. 3, n°2, p. 434–443. Copyright (2020) Wiley. (d) scanning electron microscope images of a homogeneous micromodel used for drainage experiments, adapted from Morais *et al.* (2016)⁴⁶.

Based on such systems, it is possible to play on the porosity and the permeability of the micromodel, while providing information on single or multiphase flow. Such results obtained with this kind of purposefully simplified micromodels can later be implemented in more complex simulation models.

Towards more realistic geometries. The second family of micromodels benefits from designs extracted from real rocks materials. Indeed, to access more representative rock pore geometries, it is possible to mimic native porous media. To do so, the first step generally consists in characterizing real porous

minerals to obtain 3D images with direct imaging methods such as:⁶¹

- Micro-computed tomography (micro CT)⁶² or X-ray computed tomography (XCT) techniques.⁶³
- Focused Ion Beam combined with Scanning Electron Microscope (FIB-SEM) or Transmission Electron Microscope (FIB-TEM).
- Indirect imaging methods like small-angle neutron and X-ray scattering (SANS and SAXS).⁶⁴
- Fluid invasion methods (high-pressure mercury intrusion (MICP)⁶⁵ or low-pressure adsorption (LPA) with gas like N₂ or CO₂), as well as Nuclear Magnetic Resonance (NMR) imaging.

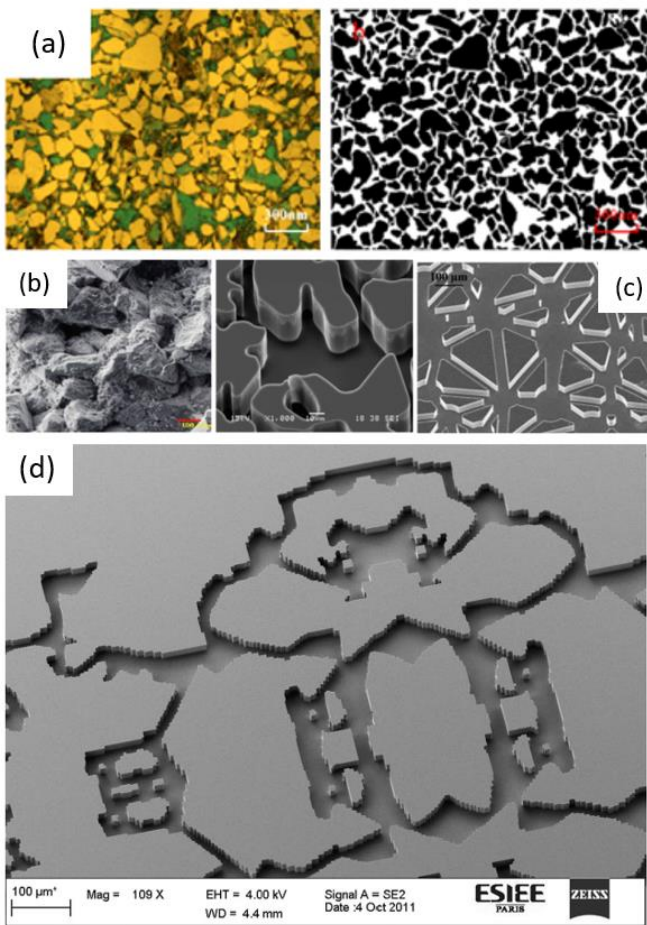


Fig. 3 (a) micrographs of a sandstone core and the associated binary image obtained from the micrographs, which is used to generate the 2D mask,⁴⁷ adapted with permission from Zuo L., Zhang C., Falta R. W., Benson S. M. Micromodel investigations of CO₂ exsolution form carbonated water in sedimentary rocks. *Advances in Water Ressources* 2013, vol. 53, p. 188-197. Copyright (2020) Elsevier. (b) SEM image of a Berea sandstone thin section and the corresponding etched micromodel⁴⁴, adapted with permission from Buchgraber M., Kovsek A. R., Castanier L. M. A study of microscale gas trapping using etched silicon micromodels. *Transport in Porous Media* 2012, vol. 95, n°3, p. 647-668. Copyright (2020) SpringerNature. (c) SEM image of pores and throats for a network fabricated from a pattern generated with a Delaunay triangulation,⁶⁶ adapted with permission from Joseph J., Kumar Gunda N. S., Mitra S. K. On-chip porous media: porosity and permeability measurements. *Chemical Engineering Science* 2013, vol. 99, p. 274-283. Copyright (2020) Elsevier. (d) SEM images of a sucrosic dolomite micromodel⁶⁸, adapted with permission from Rufai A., Crawshaw J. Micromodel observations of evaporative drying and salt deposition in porous media. *Physics of Fluids* 2017, vol. 29, p. 126603. Copyright (2020) Elsevier.

These methods do not provide information about pore size distribution but a corresponding micromodel pattern can be

generated using a Delaunay triangulation routine in Matlab[®] and/or AutoCAD[®] or a stochastic random network generator⁶⁶⁻⁶⁸ (**Fig. 3**).^{44, 47, 66, 68}

Based on the generated masks, several strategies are employed depending on the required complexity needed for the experiments. In order to mimic the topology of a saline aquifer, Buchgraber *et al.*⁶⁹ developed a representative dual porosity micromodel. This micromodel is based on the conversion of a typical Arab-D carbonate thin section into binary images, and then etched on a silicon wafer through a mask. They obtained micromodels simulating an overall porosity of 46 % including some local regions with microporosity (11 %) and other areas with local porosity values (74 %).

After microfabrication, the Microsystems consist in pore networks etched at a constant depth (2D-like model) or by varying depth.^{70, 71} As the quasi 3D nature of the pore for the latter, this kind of micromodel can be called “2.5D model”. Crandall *et al.*⁷² used the stereo lithography process, developed by Hull in the eighties⁷³ to fabricate a 2.5D micromodel. Similarly, Park *et al.* developed a process to create 2.5D SU-8 based micromodels containing up to thirteen 5 µm layers (**Fig. 4(a)**).⁷⁴

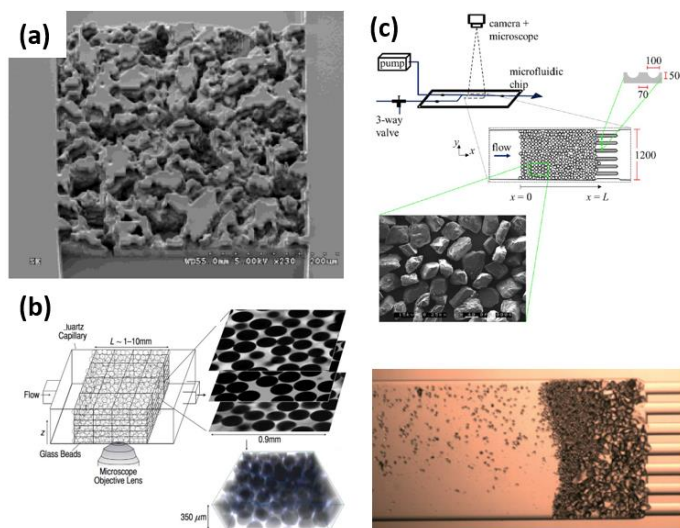


Fig. 4 Example of 2D+ micromodels geometries. (a) 2.5 D obtained from multilayers processing⁷⁴, adapted with permission from Park D.S., Upadhyay J., Singh V., Thompson K. E. Nikitopoulos. Fabrication of 2.5D rock-based micromodels with high resolution features. *Proceedings of the ASME 2015 International Mechanical Engineering Congress and Exposition IMECE2015*, November 13-19, 2015, Houston, Texas, 2015, vol. 10, p. IMECE2015-50657. Copyright (2020) ASME. (b) and (c) 3D porous micromodels obtained from the fabrication of non-consolidated packed inside a cavity,⁷⁸ (adapted with permission from Krummel A. T., Datta S. S., Münster S., Weitz D. A. Visualizing multiphase flow and trapped fluid configurations in a model three-dimensional porous medium. *AIChE Journal* 2013, vol. 59, n°3, p. 1022-1029. Copyright (2020) Wiley) or a microchannel, including multi-size and mineralogical particles,⁷⁹ (adapted from Bowden S.A., Tanino Y., Akamairo B., Christensen. Recreating mineralogical petrographic heterogeneity within microfluidic chips: assembly, examples, and applications. *Lab on Chip* 2016, vol. 16, n°24, p. 4677-4681. Creative Commons Licence - Published by The Royal Society of Chemistry) and⁸⁰ (adapted from Tanino Y., Zacarias-Hernandez X. and Christensen M. Oil/water displacement in microfluidic packed beds under weakly water-wetting conditions : competition between precursor film flow and piston-like displacement. *Experiments in Fluids*, 2018, vol. 59, p. 35. Creative Commons Licence - Published by SpringerNature).

It is also possible to add 3D aspects by etching different depths leading to micro- and macro-pore sizes. Indeed, as determined by Yun *et al.*⁷⁵, there is a change in porosity between the two fabrication procedure, the dual-depth micromodel porosity being lower than the one for the single-depth porosity. This concept demonstrated the impact of the height-to-width aspect ratio of cross section channels on the fluids behaviors. These strategies can help overcoming the constant height limitations of 2D micromodels.

So far 2D and 2.5D micromodels are the most used ones for multiphase flow displacement experiments because of the easiness of visualization and the possible of spectroscopic tools integration. However, while 2D and 2.5D micromodels are used to visualize CGS processes at the pore scale in the porous media, the design of 3D porous media could be more representative of the complex properties of real porous media, including 3D fluid flows. To achieve such 3D micromodels, several studies reported the intercalation of packed beds of solid inert beads or minerals particles either between two glass plates,^{76, 77} into a quartz capillary (**Fig. 4(b)**)⁷⁸ or inside a microfluidic channel containing or not a pre-etched structure (**Fig. 4(c)**).⁷⁹⁻⁸¹

Obviously, the main difficulty of the 3D micromodels concerns the visualization of the flow behavior since the packed material are generally not transparent anymore to visible light but to ensure an index match between the packed materials and the fluid. Therefore, while such strategies would be advantageous to match with more realistic description of the mechanisms involved in CO₂ geological storage, there are still lacking from experimental developments (in particular characterization means) and could possibly lead to complex interpretation of the results – similarly to core flood experiments. This is typically not the purpose of “micromodels” experimentation aiming at simplifying and disconnecting the multiple involved phenomena for a better understanding of each.

2.3. Playing on wettability

The wettability of the reservoir is a key factor in the behavior of multiphase flows occurring with the CO₂-brine-rock systems and therefore, control the overall CO₂ storage capacities of a reservoir.⁸² It is thus very important to be able to vary the wetting properties of a micromodel to study the impact at the pore scale of a change in wettability.⁸³ The CO₂-wettability of a mineral surface is strongly increasing with pressure, salinity or dissolved ions valency. *Defacto*, the mineralogy and the pressure can have a strong impact on contact angles values.⁸⁴

Most of the reported studies so far have been performed within water-wetted micromodels since this wettability is due to the intrinsic properties of glass and can be easily obtained for silicon using an oxidation before the anodic bonding step.²⁵ Other studies have used the largely available surface chemistry to render the micromodels’ surface either hydrophobic or to display intermediate wettability. The first one can be obtained thanks to a self-assembly monolayer (SAM) process using the silane chemistry. Various alkyl trichlorosilanes (or trimethoxy silanes) can react with the surface of glass or silicon micromodels to provide stable covalently bonded SAM leading to uniform hydrophobic wettability properties.⁸⁵ Similarly, Hu *et*

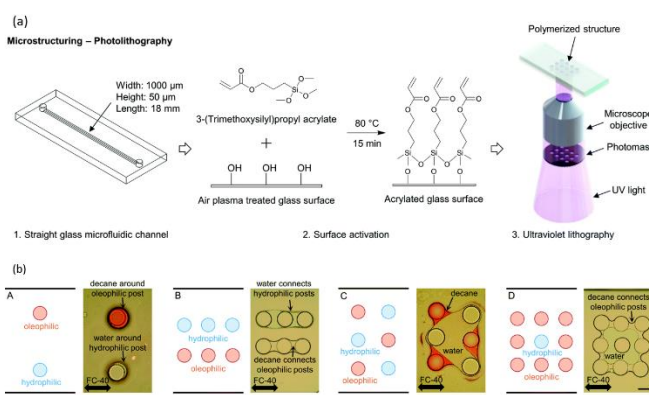


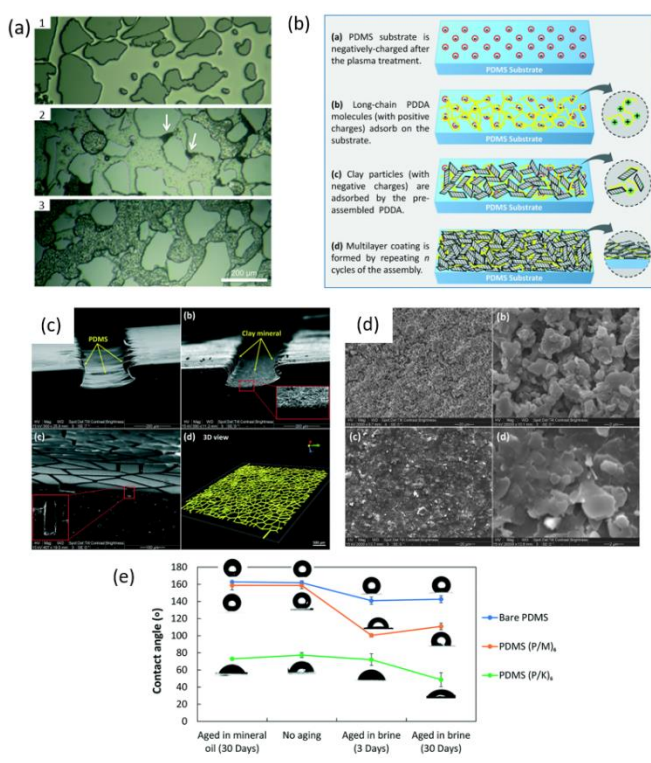
Fig. 5 (a) Schematic showing the photolithography process. Surfaces of a microchannel are activated with acrylate for fixing polymerized structures, and then the channel is filled with a UV-curable precursor solution. A microstructure is synthesized with photomask-defined geometry by UV exposure. The uncured precursor solution is removed by flushing with acetone. Then, the hydrophilic or oleophilic structures are designed and built by UV-initiated copolymerization. The degree of hydrophilicity and oleophilicity is tailored by adjusting the composition of crosslinker and monomer. (b) Mixed wettability micromodels with different arrangement of hydrophilic and oleophilic posts designed in the same microchannels. The images show the wettability behaviors of different immiscible fluids injected into the channels (water – decane – fluorinated oil - FC40).⁸⁹ (adapted from Lee H., Lee S. G., Doyle P. S. Photopatterned oil-reservoir micromodels with tailored wetting properties. *Lab on Chip* 2015, vol. 15, n°14, p. 3047-3055. Creative Commons Licence - Published by The Royal Society of Chemistry).

al.^{86, 87} treated a silica fused chip with a dilution of Aquaphobe-CM in hexane and estimated that the contact angle change from 22.4° to 89.5°. Other strategies to control the wettability properties concern weak bonding of molecule to a glass or a silicon surface. For instance, the injection of a solution of hexadecyltrimethylammonium bromide (C₁₉H₄₂BrN) in hexane solvent for 24 h with further thermal treatment provides wettability alteration to the micromodels.⁶⁹ An intermediate wettability can also be obtained by aging a sample of crude oil at 60°C during several days into the micromodel.⁸⁸

All these methodologies provide homogeneous variations of the wettability inside the full micromodels, whereas wettability heterogeneities can be more representative of realistic porous media. To achieve such complex wettability patterns within micromodels, Lee *et al.*⁸⁹ demonstrated a new method by fabricating photo patterned copolymerized microstructures using a single step UV lithography process activating a glass surface with 3-(trimethoxysilyl) propyl acrylate (**Fig. 5(a)**). Then different monomers and crosslinkers can be surface photopolymerized depending on desired wettability, *e.g.* 3-(acryloyloxy)-2-hydroxypropyl methacrylate (AHM) and 2-hydroxyethyl acrylate (HEA) for hydrophilic surface and 1,6-hexanediol diacrylate (HDDA) and lauryl acrylate (LA) for oleophilic structures. This approach is simple, fast and provides a great flexibility for generating wettability heterogeneities of the porous media thanks to the microscope stage control and the photomask designed (**Fig. 5(b)**).

2.4. Reactive microfluidic devices integrating geochemical effects

In order to account for geochemical effects along with hydrodynamics, several research teams demonstrated the integration of reactive surfaces within micromodels. The coating of micromodels’ surfaces by rock minerals leads to a change of



wettability. Song *et al.* developed a Si/Pyrex micromodel in which montmorillonite and kaolinite (clays minerals) were deposited.^{90, 91} The kaolinite was chosen because of its prevalence in Berea sandstone, and to further study the release of fine clay particles during EOR process.^{92, 93} By mixing the mineral powder with a high salinity brine solution, the risk of plugging is reduced and the clay particles adsorption on the silica surface is promoted (**Fig. 6(a)**). This approach was also demonstrated for brucite minerals.⁴⁸

The layer-by-layer (LbL) assembly is yet another technology that can also be used to produce rock minerals coatings to mimic the subsurface mineralogy. Zhang *et al.*⁹⁴ developed “Surface-Mimetic Micro-Reservoirs (SMMR)” with representative clay pores of sandstones and mudrocks reconstructed with montmorillonite and kaolinite coating onto PDMS and glass

surfaces (**Fig. 6(b)-(e)**). This results in the formation of a stable mineral surface with tunable wetting properties.

Another way to fabricate synthetic CaCO₃ reservoir micromodels is to process an *in situ* growth of CaCO₃ nanoparticles by photo-patterning. Lee *et al.*⁹⁵ developed a method to create large area of tunable CaCO₃ microfluidic microarrays. They obtained a wider range of topographies and geochemical properties than with a classical micromodel, in particular in terms of wettability, geometry and porosity (**Fig. 7**). Whatever the considered deposition process, the aging of the coated CaCO₃ permits to tune the wettability of the surface in order to simulate reservoir conditions.⁹⁶

Recently, some research groups developed alternative technologies involving aiming at fabricating the model geological labs on a chip directly from real geo-materials. For instance, Porter *et al.*⁵⁷ reported a micromodel fabrication method combining both geo (shale, siltstone, sandstone) and engineered (glass) materials (**Fig. 8(a)-(b)**). This consists in a thin section cut from a larger rock core, which is later UV-epoxied to a glass plate (quality quartz microscope slides). 3D tomography images of real fractures are used to mimic the pore space and fracture geometries of the subsurface formations. Thus, the patterns are etched into the micromodels with a Gravograph laser (LS 100 – 40 W) or a femtosecond laser direct write (LDW). The control of the depth and the roughness of the etched pattern is ensured by the laser operating parameters and this for each material. This technology allows them to directly observe reactive flows and transport behavior at reservoir conditions.

Similarly, Song *et al.* reported the fabrication of a real-rock micromodel with microchannels etched directly in a natural calcite crystal sealed with a glass slide.⁵⁸ This method provides the advantages of using relevant substrate chemistry and the real time pore-scale resolution. The microfabrication method is shown in **Fig. 8(c)**. First, a 3 mm thick wafer, previously cut from a large calcite crystal, is coated with a layer of beeswax. Then, a pattern is etched in into the wax with a laser cutter. Finally, the

channels are etched using hydrochloric acid (HCl) and the wax is removed. To seal the micromodel, the cleaned etched surface is bonded to a borosilicate glass side with a thin layer of adhesive. The channel shape depends on the crystallographic planes, leading to a half-trapezoidal cross sectional geometry

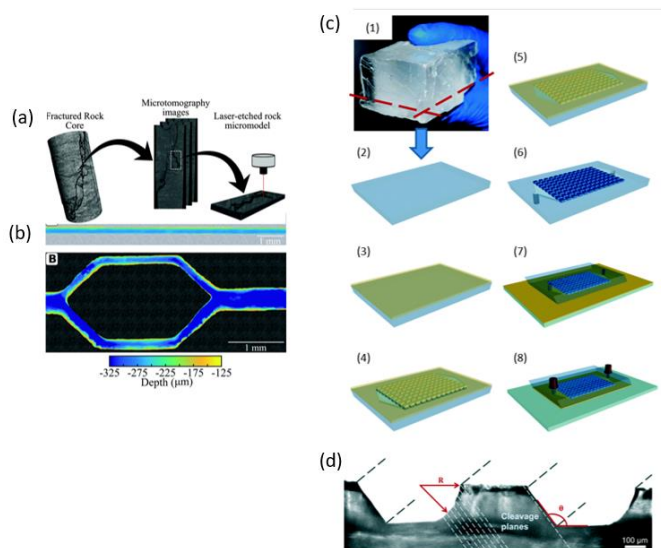


Fig. 8 (a) Illustration of the concept for the geo-materials micromodel fabrication. (b) Profilometer depth measurements of (top) a straight channel etched in cement using the CINT laser and (bottom) a pore doublet etched in shale using the Gravograph laser.⁵⁷ (adapted with permission from Porter M. L., Jiménez-Martínez J., Martínez R., McCulloch Q., William H. S. Geo-materials microfluidics at reservoir conditions for subsurface energy resources applications. *Lab on Chip*, 2015, vol. 15, n°20, p. 4044-4053. Copyright (2020) The Royal Society of Chemistry.). (c) Natural calcite micromodel. A large calcite crystal (1) is cut into thick wafers (2) and coated with a thin layer of beeswax (3). The pattern is etched through the wax using a laser cutter (4) and then etched through the calcite crystal with hydrochloric acid (HCl) (5). The wax is removed and the inlet and outlet ports are drilled into the crystal (6). Once the etched calcite is bonded to a glass plate with an adhesive (7) nanoports are attached to connect the micromodel to the fluid systems. (d) Cross section of the channels etched through the calcite crystal.⁵⁸ (adapted with permission from Song W., de Haas T. W., Fadaei H., Sinton D. Chip-off-the-old-rock: the study of reservoir-relevant geological processes with real-rock micromodels. *Lab on Chip*, 2014, vol. 14, n°22, p. 4382-4390. Copyright (2020) The Royal Society of Chemistry.).

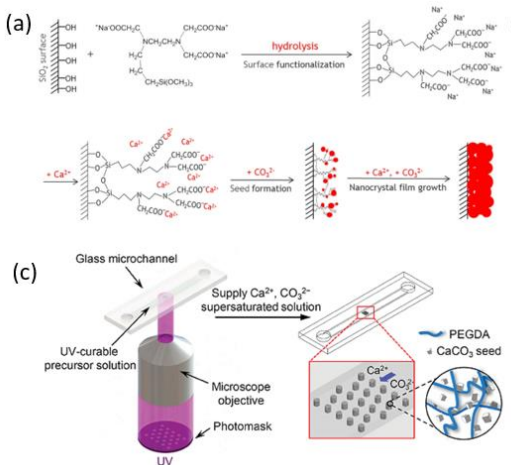


Fig. 7 (a) Schematic illustration of surface modification by silane and seeded growth of calcium carbonate nanocrystals on glass. (b) Photograph of a glass microfluidic chip and cross section SEM images of CaCO_3 nanocrystals coating on the surface of microchannels of the chip at different magnifications and focus areas,⁹⁶ (adapted with permission from Wang W., Chang S., Gizzatov A. Toward Reservoir-on-a-Chip: fabricating reservoir micromodels by *in-situ* growing calcium carbonate nanocrystals in microfluidic channels. *ACS Applied Materials & Interfaces* 2017, vol. 9, p. 29380-29386. Copyright (2020) American Chemical Society). (c) Schematic illustration showing the photolithographic patterning and the subsequent in situ growth of the CaCO_3 . (d) SEM images of the outer side surface of the composite posts with different growth time, (e) growth of CaCO_3 posts with heterogeneous structures.⁹⁵ (adapted with permission from Lee S.G., Lee H., Gupta A., Chang S., Doyle P. S. Site-selective *in situ* grown calcium carbonate micromodels with tunable geometry porosity, and wettability. *Advanced Functional Materials* 2016, vol. 26, n°27, p. 4896-4905. Copyright (2020) Wiley).

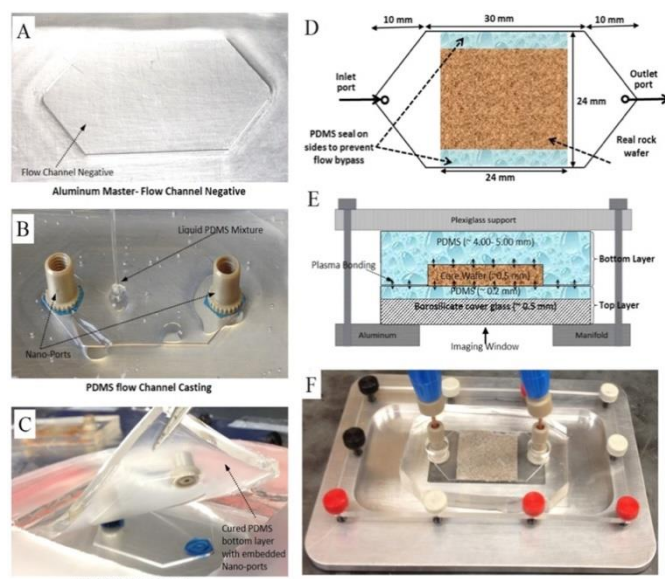
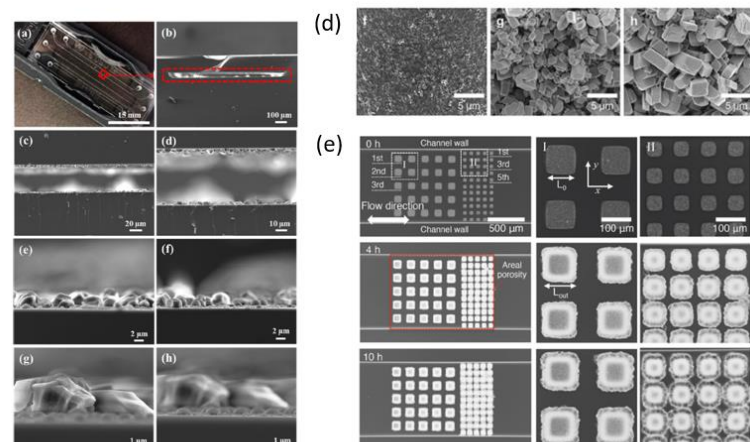


Fig. 9 Design and fabrication images of the microfluidic flow channel and the Real Rock-Microfluidic Flow Cell (RR-MFC) assembly. A) Lathe machined flow channel negative aluminum master on which B) liquid PDMS was poured to mold the flow channel along with nano-ports imbedded into it. C) Solidified PDMS channel after heat curing at 70 °C for 2 h. Schematics showing D) top and E) cross-sectional views of the rock wafer assembly inside the PDMS/aluminum manifold. The flow direction in image E is perpendicular to the plane of the page. F) Complete RR-MFC assembly. Note that the RR-MFC in images E-F are viewed upside down and thus the top imaging plane of the rock wafer is at the bottom.⁹⁷ (adapted with permission from Singh R., Sivaguru M., Fried G. A., Fouke B. W., Sanford R. A., Carrera M., Werth C. J. Real rock-microfluidic flow cell: a test bed for real-time *in situ* analysis of flow, transport, and reaction in a subsurface reactive transport. *Journal of Contaminant Hydrology* 2017, vol. 204, p. 28-39. Copyright (2020) Elsevier).

(Fig. 8(d)) parallel to the cleavage planes of the calcite crystal (with $\theta = 125^\circ$) and a rounded edge on the side in which the etching direction is orthogonal to the cleavage planes (with R on the order of the channel depth).

It is also possible to work directly with a thin slice of rock material, and thus to obtain a realistic dynamic flow-through experimental platform to study reactive transport at small scales.⁹⁷ An example from Singh *et al.*⁹⁷ is shown in **Fig. 9**, so



called Real Rock-Microfluidic Cell (RR-MFC), made from a 500 μm -thick rock wafer from the Clair Group sandstone integrated to a PDMS microreactor. It provides more realistic reactive flow conditions compared to classical microfabricated chips.

3. How to characterize the phenomena at the pore scale?

Given that CO₂ storage involves coupled phenomena including fluid flow in porous medium, geochemistry and bio geology, it is critical to choose the right characterization technique to access the targeted information. We introduce in this section the most commonly considered characterization techniques coupled to high pressure microreactors^{98, 99} and micromodels for investigating the mechanisms involved in CO₂ geological storage.

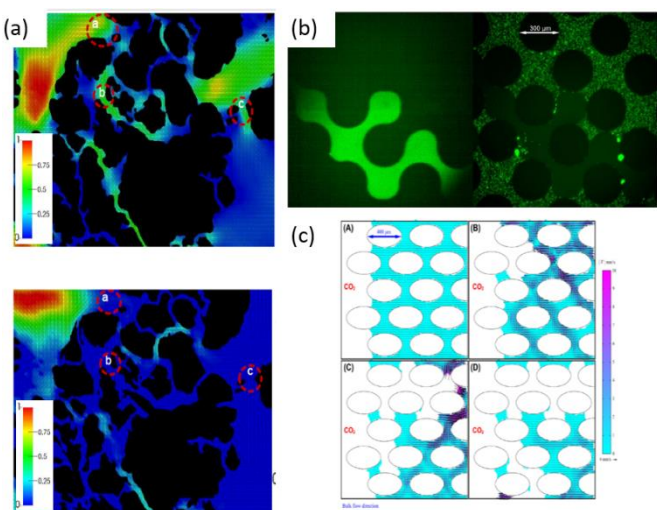


Fig. 10 (a) Normalized magnitude of velocity from μ -PIV for single- (top) and dual-depth (bottom) dual-porosity micromodels at interstitial velocity of 1 m/day with water injection rate (0.0008 ml/min). Flow direction is from left to right. Single-depth micromodel has pore throat dimensions (width by depth) of the circled locations with constant etch-depth: a (30 μm by 14 μm), b (12 μm by 14 μm), and c (15 μm by 14 μm). Dual-depth micromodel has pore throat dimensions (width by depth) of the circled locations where a holds constant etch-depth, but b and c have reduced etch depth: a (30 μm by 14 μm), b (12 μm by 7 μm), and c (15 μm by 7 μm).⁷⁵ (Reprinted with permission from Yun W., Ross C. M., Roman S., Kovscek A. R. Creation of a dual-porosity and dual-depth micromodel for the study of multiphase flow in complex porous media. *Lab on Chip*, 2017, vol. 17, n°8, p. 1642-1647. Copyright (2020) The Royal Society of Chemistry.). (b) Double visualization of CO₂ drainage: (left) dyed CO₂ image and (right) Tracer particle image.⁴⁵ (Reprinted with permission from Kazemifar F., Blois G., Kyritsis D. C., Christensen T. A methodology for velocity field measurement in multiphase high-pressure flow CO₂ and water in micromodels. *Water Resources Research* 2015, vol. 51, n°4, p. 3017-3029. Copyright (2020) Wiley.). (c) Velocity vector fields during finger formation ($t = 6.4\text{--}6.7 \text{ s}$, t between frames = 100 ms). A. Frame 65. B. Frame 66. C. Frame 67. D. Frame 68. Velocity jumps clearly evident in C ahead of the growing finger (80 bar, 40 °C, 0.005 ml/min).¹¹¹ (Reprinted with permission from Kazemifar F., Blois G., Kyritsis D. C., Christensen T. Quantifying the flow dynamics of supercritical CO₂ – water displacement in a 2D porous micromodel using fluorescent microscopy and microscopic PIV. *Advances in Water Resources* 2016, vol. 95, n°4, p. 352-368. Copyright (2020) Elsevier.).

3.1. Optical observations

As mentioned in the previous section, most of the micromodels developed for investigating CO₂ geological storage at the pore scale are transparent and therefore possess an optical access. This can be used to monitor the imbibition or drainage process and to

investigate possible preferential pathways along with reactive flows, including dissolution or precipitation processes. The optical access provides the ability to determine in real time the saturation level by creating binary images. Indeed, the CO₂ and the brine phases exhibiting a different refracting index of the light, they can be thus distinguished.^{44, 46, 100, 101} In the case of minerals precipitation, fluorescein-dyed brine can also be injected to improve the detection and to evaluate the effects of precipitation on the flow,^{43, 102} using an epifluorescent microscope.⁵¹ Besides the aqueous phase, the CO₂ phase can also be dyed using the addition of Coumarin 153 or Nile red without any alteration of the fluid properties such as its viscosity, its density nor the wettability.^{51, 52, 103, 104} The fluorescent signal intensity of the dyed phases helps distinguishing both the solid materials of the microsystem, the two phases and the ongoing mineral precipitation. Similar strategies can be applied to reactive micromodels made of real minerals to monitor fluid displacement in 3D using confocal laser microscopy.⁹⁷ Some dye such as fluorescein can also be used to access supplementary information about pH. Indeed, at acidic pH, the fluorescent of fluorescein is quenched¹⁰⁵ giving the ability to literally “visualize” the CO₂ dissolution in water, which leads to an acidification of the aqueous phase.^{106, 107}

Fluid flow and velocity profile inside porous medium are yet other critical information to improve the understanding of CO₂ trapping mechanisms when geometrical considerations are taken into account, especially velocity field variations in reactive porous structures. To access these data, μ -Particle Image Velocimetry technique (μ PIV)¹⁰⁸ and anemometry¹⁰⁹ are common techniques to investigate velocity profiles within a micromodel. The fluid is seeded with small tracer particles and their motion is tracked to deduce the fluid motion.¹¹⁰ Yun *et al.* used this technique to highlight the change in terms of velocity field for their dual porosity models compared to the single-depth ones (Fig. 10(a)).⁷⁵ Similarly, Kazemifar *et al.*^{45, 111} directly extracted the CO₂ flow velocity in a water-filled porous media during the drainage process (Fig 10(b)-(c)).

Despite the interest of optical visualization techniques, no direct bio-geochemical information can be provided in the visible light range. Although several microbiology techniques allow accessing critical *in situ* information on cells using UV-visible light (Fluorescence *In Situ* Hybridization – FISH, live and dead kits, etc.) they require the use of markers. Besides, such approaches are specific to microbiology and cannot be used more generally to investigate geochemical effects. Therefore, in here, we purposefully focus only on non-intrusive characterization techniques. To do so, several research works have focused on spectroscopy (Raman and Infrared) to investigate solubilization processes or chemical reactivity and precipitation processes inside micromodels.

3.2. Spectroscopy approaches

Raman and Infrared spectroscopy are non-intrusive techniques giving access to chemical vibrations modes of molecules, therefore providing information on bio-geochemistry occurring

during CO₂ geological storage processes. When considering micromodels experiments, such approaches are generally coupled to microscopy to attain the adapted space resolution and possibly to proceed with spatial chemical mapping / imaging. Note, however that the construction materials of the micromodels drive the choice of the characterization technique to use. For instance, although Pyrex is transparent in the visible range and therefore compatible with *in situ* Raman spectroscopy, it is not transparent in the IR range, restricting the use of FTIR spectroscopy.¹¹²

Raman spectroscopy. Confocal Raman microspectroscopy is an outstandingly efficient characterization technique for *in situ* investigation at the pore scale. So far, its use has been reported for investigations related to two aspects of the geological CO₂ storage: the solubility trapping and the mineral trapping. Liu *et al.* used the confocal Raman spectroscopy (with a 532 nm wavelength excitation laser) to determine the CO₂ solubility in water and brine in a HP/HT micromodel.⁵³ Indeed, the use of the peak intensity ratio between an aqueous CO₂ Fermi dyad band (\sim 1385 cm⁻¹) and the water stretching band (\sim 3480 cm⁻¹) associated with third order polynomial models¹¹³ can be used to access the solubility of CO₂ in pure water or in brine for NaCl concentrations (Fig. 11) directly on a chip.

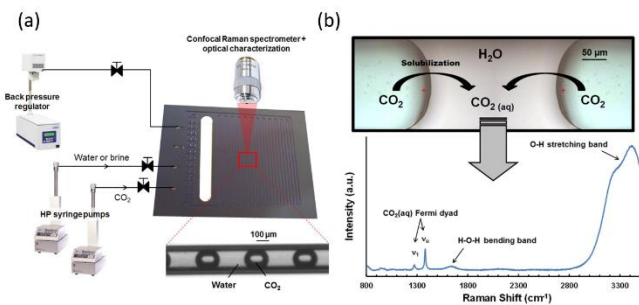


Fig. 11 (a) Experimental setup with a Si/Pyrex micromreactor connected to high pressure pumps, a back-pressure regulator and the Confocal Raman spectrometer. (b) Optical image of a CO₂/water interface and corresponding confocal Raman spectra of CO₂ dissolved in water, adapted from Liu *et al.* (2012)⁵³.

A backscattering Raman spectroscopy can also be used to characterize crystal polymorphs. For instance, the collect of the 100-2000 cm⁻¹ spectra allows capturing the entire range of CaCO₃ polymorphs (vaterite, aragonite and calcite) as well as magnesium containing minerals (dolomite and magnesite). Other studies have reported the use of Raman spectroscopy to investigate other minerals such as α -quartz (with characteristics peaks located at 128, 206, 265, 355, 401, 464 cm⁻¹),¹¹⁴ K-feldspar (157, 285, 513, 750, 813, 994 cm⁻¹)¹¹⁵ and calcite cement (156, 283, 711, 1085 cm⁻¹).^{97,116} These latest advantages allow for considering Raman spectroscopy for studying the impact of reactive flow in real rock chip configuration.

In situ Raman spectroscopy has been equally successfully used to map packed beds micromodels working under HP / HT conditions to reach molecular information about asphaltenes sheets¹¹⁷ and to study the growth of methane hydrate thin films in micromodels.¹¹⁸ These results demonstrate the Raman spectroscopy is a powerful tool to study several different phenomena related to underground conditions experiments at the pore scale.

IR spectroscopy. Although it is not straightforward to proceed with pore scale experiments with *in situ* IR spectroscopy due to the reactor microfabrication materials¹¹², despite recent developments in materials science and microfabrication¹¹⁹, the field of optical fiber sensor technologies has grown. IR-compatible fibers can be quite easily implemented in micromodels and provide the possibility to distinguish CO₂, brine and CO₂ saturated brine by using a wavelength shift of 1.149 nm^{120, 121}. Bao *et al.*¹²² validated the ability to use chalcogenide glass fibers¹²³ by distinguishing first supercritical CO₂ (40°C and 9.65 bar) and brine (3M NaCl solution), and then by demonstrating the ability to follow a CO₂ saturation of brine (with a 0.192 nm shift between the CO₂-saturated brine and the initial brine solution) (Fig. 12(a)-(c)).

Starecki *et al.*¹²⁴ then developed an *in situ* CO₂ mid-IR detection probe directly integrated within a high-pressure microsystem. It was possible to detect the presence of CO₂ at p,T conditions representative of deep aquifers thanks to an embedded rare earth doped chalcogenide fiber. When considering a dynamic mode (segmented CO₂ / water flows), a 100 ms sampling frequency was successfully achieved (Fig. 12(d)-(e)).

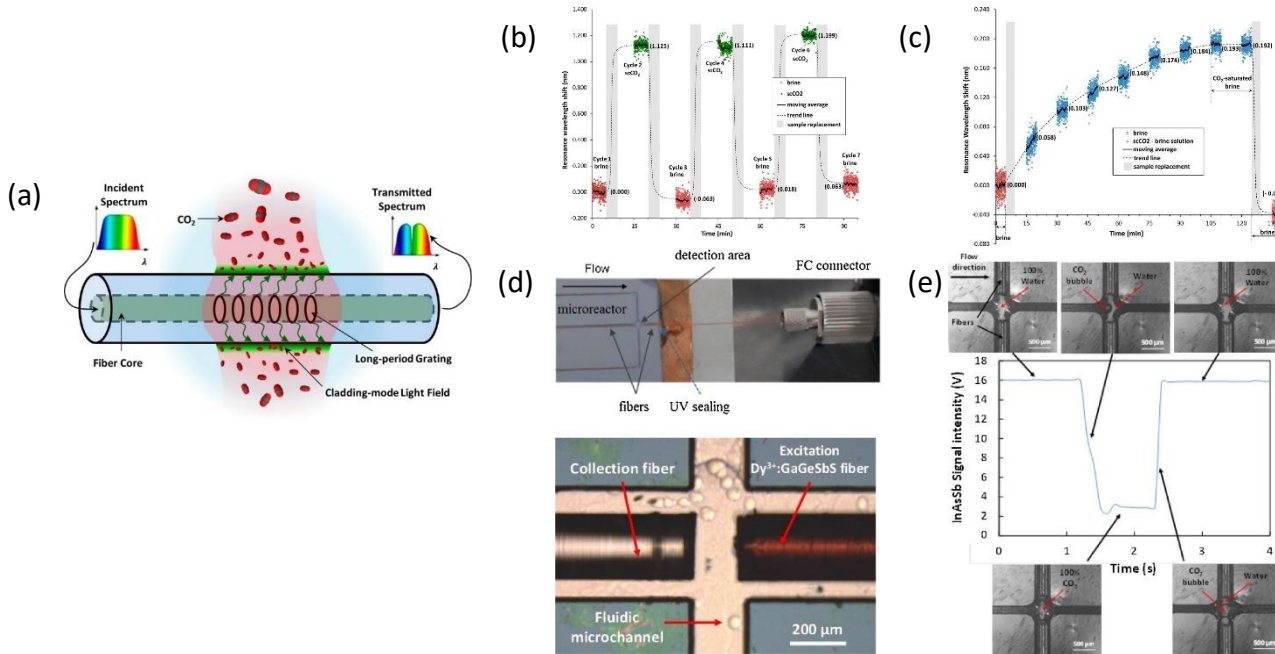


Fig. 12 (a) Scheme of the CO₂ sensing method. The flowing CO₂ creates a band attenuation of the resulting transmission spectrum (b) Alternate cycle of scCO₂ (green) and brine (red) have been performed. The spectrum highlights the 0.119 nm shift of the resonance wavelength. (c) The resonance wavelength shift corresponding to CO₂-saturated brine solution (blue circles) as compared to the original brine solution (red rectangles). Data are collected in 5 min periods at 15 min intervals. A moving average is plotted as a solid line, and a dashed line provides a guide for the eye between data sets. The saturation equilibrium was achieved after 100 min from t = 5 min when scCO₂-brine solution replaced the initial brine. A detectable resonance wavelength shift of 0.192 nm is observed for CO₂-saturated brine relative to the original brine solution.¹²² (Reprinted with permission from Bao B., Melo L., Davies B., Fadaei H., Sinton D., Wild P. Detecting supercritical CO₂ in brine at sequestration pressure with an optical fiber sensor. Environmental Science and Technology 2013, vol. 47, n°1, p. 306-313. Copyright (2020) American Chemical Society.). (d) Picture of a InAsSb IR fibers integrated microdevice for CO₂ and water detection and (e) InAs Sb signal intensity and optical visualization of a CO₂ bubble passing through the detection volume. Adapted from Starecki *et al.* (2016)¹²⁴.

3.3. X-Ray approaches

Pore scale view of the involved phenomena in 3D non-transparent structures (such as non-consolidated “packed bed” porous media or 3D structures involving geological materials, see sections 2.2 and 2.4) requires the use of X-Ray techniques as conventional optical or spectroscopy approaches do not allow for *in situ* visualization (similarly to core-scale experiments). Hence, the coupling between X-Rays and micromodels is critical.

X-ray diffraction. In this context, the reliability of high pressure Si/Pyrex microsystems allows the implementation of X-Ray analytic techniques such as Small-Angle and Wide-Angle X-ray scattering (SAXS/WAXS). For instance, Beuvier *et al.* conducted a study consisting in analyzing calcium carbonate (CaCO₃) precipitation in a microchannel.¹²⁵ The scattering signals of the solvent and the Pyrex cover can be distinguished from the narrow diffraction peaks of the CaCO₃. Then, the WAXS mode can provide information on the carbonate crystallographic structure (calcite, aragonite or vaterite) while the SAXS mode, acquired at the same time, provides clues about the particle size and morphology, in this case, micrometric rhombohedra of calcite for example. The glass side of the microreactor gives the ability to further confirm this information to validate the methodology through *in situ* optical imaging (**Fig. 13**).

At the pore scale, X-ray diffraction (XRD) can also be used to characterize thin rock sections¹²⁶, and it can be coupled with micro X-ray fluorescence (μ -XRF). For instance, XRD can

detect components in shale samples like quartz (SiO₂), calcite (CaCO₃), illite ((KH₃O)Al₂Si₃AlO₁₀(OH)₂), albite (NaAlSi₃O₈), microcline (KAlSi₃O₈) or pyrite (FeS₂), while μ -XRF can determine the proportion of minerals such as SiO₂, CaO, SO₃, Al₂O₃, K₂O or Fe₂O₃. This is very useful to determine the mineral reactivity of a rock sample inserted into a microfluidic chip toward a reactive fluid like brine or waste water.

X-ray μ CT. The X-ray μ CT is already used for rock samples in order to quantify *in situ* wettabilities¹²⁷ or to study CO₂ exsolution in sandstone.¹²⁸ The μ CT is also used complementary to magnetic resonance imaging (MRI) to study advection, dispersion and the formation of precipitate in 3D porous media flow cells.^{129,130} Indeed, MRI gives special mapping information of local velocity fields changes and dispersion in the sample, while μ CT permits the visualization of precipitation into the porous media.

In brief, several *in situ* and noninvasive characterization techniques are readily available to investigate CO₂ geological storage associated mechanisms. This can be done in confined environment at the pore scale in realistic pressure and temperature conditions both from a hydrodynamics and geochemical point of view. These characterization tools have been applied to several reported studies, which are detailed in the next section.

4. Geological Labs on Chip for the discovery of (bio)geochemistry and physics

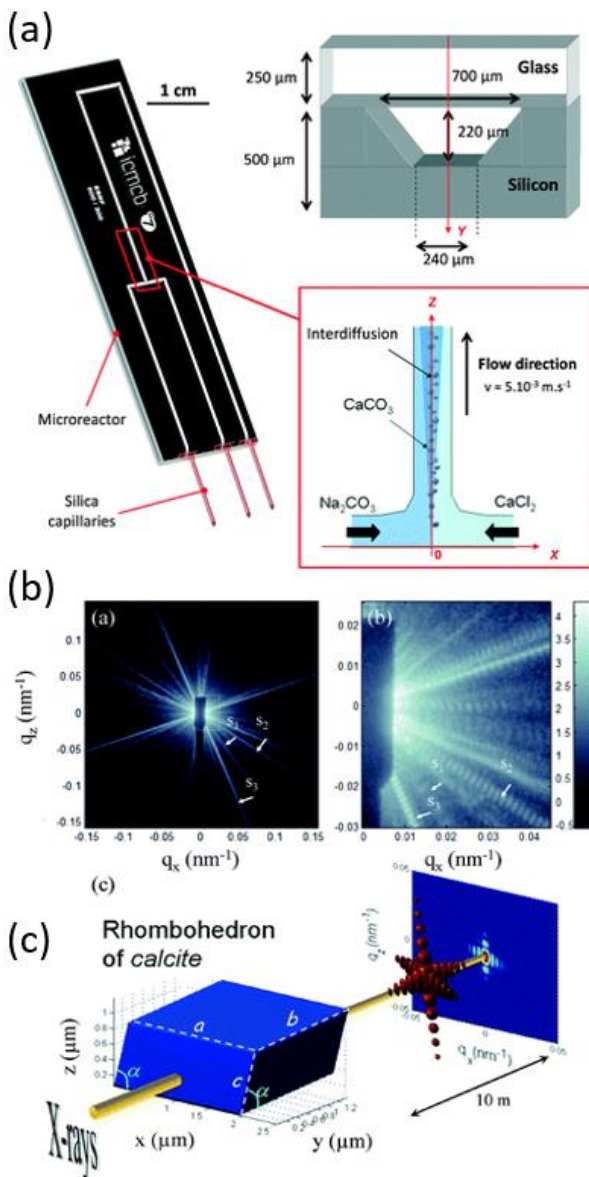


Fig. 13 (a) General view and details of the microreactor used for the SAXS/WAXS experiments. (b) Example of SAXS images acquired during the experiments. The streaks s_1 , s_2 and s_3 are attributed to the presence of microcrystals of calcite precipitated into the microreactor. The scheme (c) shows the rhombohedron of calcite and its related scattered intensity. Adapted from Beuvier *et al.* (2015).¹²⁵

Most of the reported studies investigating CO₂ geological storage at the pore scale have been focused on four main mechanisms, namely: (i) invasion processes and capillary trapping, (ii) solubility measurement and trapping, (iii) minerals dissolution / precipitation and (iv) biogeochemical effects.

4.1. Fluid flow in porous media: Capillary trapping

Permeability measurement and its effect on drainage and imbibition processes. The permeability of a micromodel depends on the porosity and the depth of the etched patterns. In most cases, the greater the etched depth is, the greater the permeability of the porous media is (same for the porosity).⁶⁹

Experimentally, the absolute permeability is estimated by measuring the pressure drop across the porous media (typically

with low differential pressure transducers) during an injection of water.¹³¹ For the absolute permeability measurement of their Reservoir On a Chip (ROC), Joseph *et al.*⁶⁶ used the Darcy law¹³²:

$$K = \frac{Q \times \mu \times L}{A \times \Delta P_{FD}}$$

Where K is the absolute permeability, Q is the flow rate, μ is the viscosity of the water, L is the length of the micromodel, A is its cross section (*width* \times *height*) and ΔP_{FD} is the pressure drop across the ROC. In most cases, a $\Delta P = f(Q)$ is plotted and the slope is used to calculate the permeability.

The complexity of the aquifer's porous media, however, leads to the consideration of other factors. Joseph *et al.*⁶⁶ demonstrated that for two networks with similar depth and porosity, the permeability changed with the number of pores and throats. Macroscale experiments have already shown that CO₂ will preferentially displaced water through areas with higher permeability values.^{133, 134} Zhang *et al.* confirmed this phenomenon by a direct observation of water drainage by liquid CO₂ in a Si/Pyrex micromodel with a dual-permeability etched network.⁵¹ The area exhibiting the lower permeability value could be efficiently drained if the capillary number reached a certain value ($\log Ca = -3.36$). They identified three types of CO₂ phase morphologies: mobile phase, large multipore blobs and small blobs. With this denomination, they showed that the higher the capillary number, the more important was the mobile phase, identifying a dominance of the capillary fingering for the lower injection rate and a viscous fingering for the higher injection rates (Fig. 14(a)). The CO₂ phase saturation also increases with the injection rate. The proportion of CO₂ in the low permeability area is an important parameter to determine the efficiency of a sealing caprock. Other studies investigating viscous and capillary fingering reported the crossover from capillary fingering to viscous fingering in a rough fracture.¹³⁵

Cao *et al.* showed the link between the microscopic geometry and the relative permeability of the reservoir, by associating the capillary trapping of small bubbles in narrow pore throats to the decrease of the relative permeability.⁵⁶ For such an investigation, the μ PIV technique is useful to determine the velocity of CO₂ into water-filled micromodel. In particular, three flow stages have been reported:¹¹¹

- A pre-front passage consisting of a flow with periodic features before the CO₂ actually enters the micromodel
- A front passage which is the actual appearance and migration of the CO₂ front
- A post front passage relative to the evolution of the flow field after the passage of CO₂ front.

During the front passage stage, sudden and rapid growths of CO₂ dendritic features (fingering) were observed. The local CO₂ velocity in such hydrodynamic structures can reach values as high as 20-25 times higher than the bulk one, supporting the notion of Haines jumps during front propagation due to local dynamic pressure gradients in the micromodel.¹³⁶

Besides the porosity and the permeability of the micromodels, the pore characteristics have also a strong influence on the CO₂/water displacement. Chang *et al.* studied

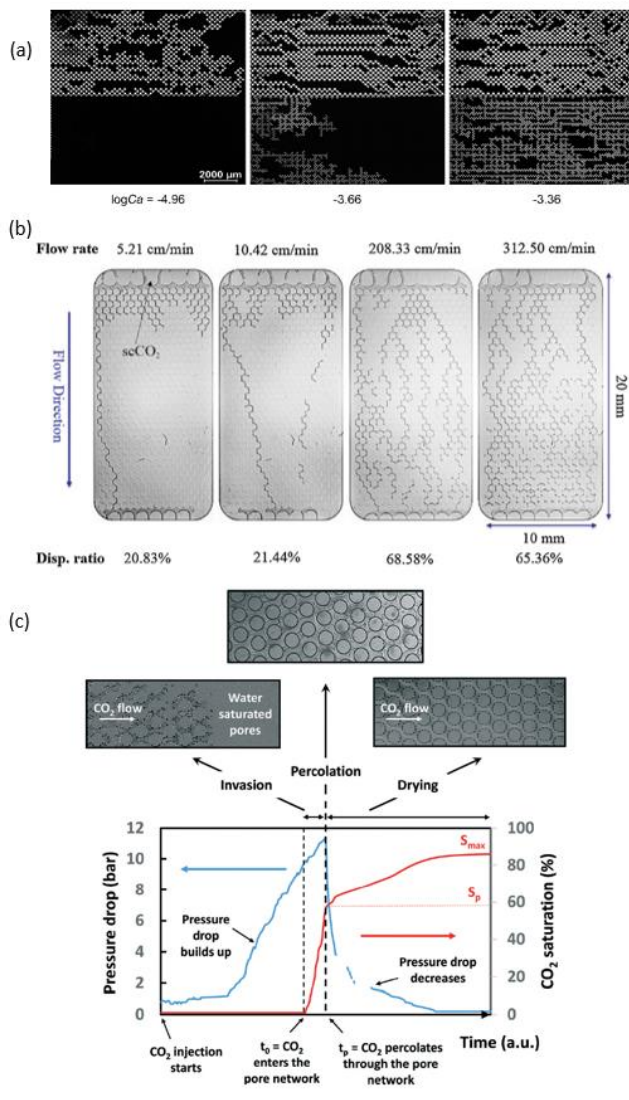


Fig. 14 (a) Liquid CO_2 (in white) distribution in the dual permeability micromodel. The Liquid CO_2 was injected at different injection rate. Higher is the velocity of the CO_2 , more it penetrates the lower permeability area⁵¹ (Reprinted with permission from Zhang C., Oostrom M., Grate J. W., Wietsma T. W., Warner M. G. Liquid CO_2 displacement of water in a dual-permeability pore network micromodel. Environmental Science and Technology 2011, vol. 45, n°17, p. 7581-7588. Copyright (2020) American Chemical Society.). (b) Supercritical CO_2 (in dark) distribution after percolation for different injection rates. The displacement ratio (the part of NaCl solution displaced) increases when the flow velocity is increasing.⁵⁶ (Reprinted with permission from Cao S. C., Dai S., Jung J. Supercritical CO_2 and brine displacement in geological carbon sequestration: micromodel and pore network simulation studies. International Journal of Greenhouse Gas Control 2016, vol. 44, p. 104-114. Copyright (2020) Elsevier.). (c) Pressure drop and CO_2 saturation as functions of time during a typical drainage process inside a micromodel (adapted from Morais *et al.* (2016)⁴⁶).

these effects with imbibition experiments into four different micromodels with varying anisotropy, heterogeneity and pore-throat aspect ratio.⁵⁴ They reported that the residual trapped CO_2 was due to a bypass phenomenon, induced by heterogeneities in pore characteristics and pore-scale sc CO_2 -water distribution. This can be overcome by having a higher transverse permeability, which will result in an enhanced sweep efficiency by reducing the sc CO_2 .

Effects of the injection methodology. In the large majority of the reported experiments concerning CO_2 invasion and drainage

in a saturated brine-filled porous medium, the unfavorable ratio (M) between CO_2 and brine leads to an unstable displacement process (refer to the log M and log Ca values for all the studies of this section reported into the Lenormand diagram (**Fig. 15**)^{22, 46, 51, 52, 54, 56, 100, 137, 138}. Therefore, several strategies have been developed to investigate the influence of the injection methodology on the final CO_2 saturation. For instance, a study with continuous and discontinuous injections of sc CO_2 in water has showed different mechanisms. For discontinuous injection rate experiments, a low injection rate led to a domination of capillary fingering (with a higher sc CO_2 saturation), whereas a high CO_2 velocity involved viscous fingering. The continuous injection always showed a capillary fingering behavior and an increase of the CO_2 saturations as the injection rates were increasing.^{52, 138} Indeed, in the most cases, the CO_2 -brine (or water) displacement increased with the capillary number Ca , improving the CO_2 injection efficiency⁵⁶ (**Fig. 14(b)**). Regarding these observations and the CO_2 viscosity and interfacial dependency of the capillary number, some optimization methods can be considered such as increasing the velocity of the flow, or the CO_2 flow viscosity (for example by adding of viscosifiers), or playing with the interfacial tension or the contact angle using surfactants.¹³⁹

Lastly, Chang *et al.*⁵⁴ demonstrated that just Lenormand's diagram and capillary number were not sufficient to account for all the invasion phenomena. Specifically, they performed experiments in different micromodels in the same range of $\log Ca$ and observed different behaviors. In particular, the crossover zone between capillary fingering and viscous fingering didn't appear for the same $\log Ca$. Their observation indicated a strong influence of the pore geometry and the pore-network topology

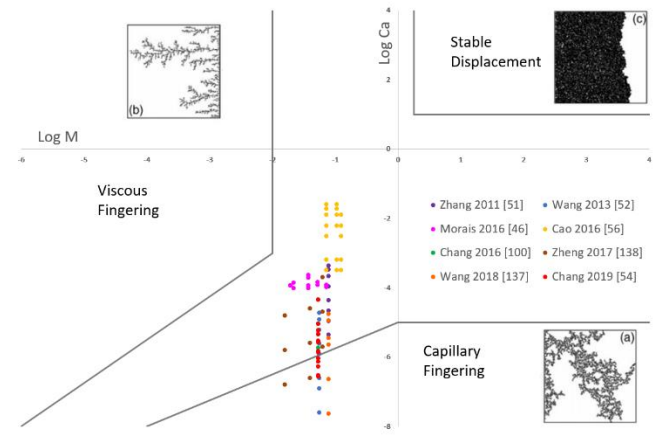


Fig. 15 Fluid invasion conditions plot used by experimental studies with water and CO_2 . The area for viscous fingering, capillary fingering and stable displacement are from the studies of Lenormand²².

on the drainage fingering. To include the geometrical effects, they define a “complete capillary number”, which takes into account the pore network characteristics in order to be able to improve the comparison between micromodels and the description of the fluid invasion.

Wettability influence. Besides the geometry, the wettability of a porous media also has a strong influence on the CO_2 -brine displacement mechanisms by its impact on interface's

stability.¹⁴⁰ Intermediate wetting properties of the porous media lead to wider fingering, more compact displacement pattern and higher CO₂ saturation. This involves that the reduction of the wettability increases displacement efficiency.^{87, 141} This highlighting is very useful to understand what can occur during geological sequestration, because of the difference in wettability of different regions of the caprock.¹⁴²⁻¹⁴⁵ Experiments with water-wet and intermediate-wet homogeneous micromodels prefilled with CO₂ showed the effect of wettability on CO₂ capillary trapping. The less water-wet pore surfaces trapped more CO₂ (+ 15% of saturation). But this additive trapping no longer exists when considering high brine flow velocities.⁸⁷ The salinity of the brine is also a key parameter to take into account, as it can strongly modify the wettability^{55, 146-148} and therefore the displacement processes. Kim *et al.*⁴⁹ showed at the pore scale the wettability alteration is due to the salinity of the brine (the contact angle increased from 0° to 80°, with an increase in the salt concentration). The study with NaCl brine confirmed this effect by featuring that higher brine salinity decreased the overall displacement (due to the increase of the contact angle between the brine and the CO₂, reducing the efficiency of the CO₂ flow).⁵⁶

Physical forms of CO₂ and water saturation. When studying CO₂ invasion processes, it is of primary importance to consider the pressure and temperature conditions, which drives the phase of the invading CO₂ phase (*i.e.* gas, liquid or supercritical). Morais *et al.*⁴⁶ highlighted the different mechanisms involved during the drainage of a water saturated porous medium by CO₂ at different physical forms. They built CO₂ curves as a function of time and distinguished invasion, percolation and drying mechanisms¹⁴⁹ (Fig. 14(c)). They observed two phenomena: water films break up, which the thickness can be determined with Bretherton's law¹⁵⁰ - a drying mechanism occurring principally with the supercritical CO₂. Both increased the efficiency of the drainage into the GLoC (Geological Lab On a Chip). On the other hand, Zheng *et al.*¹³⁸ confirmed the increase of the CO₂ saturation with an increasing capillary number for a given phase. In their experiments, liquid CO₂ showed a highest sweep efficiency due to a high viscosity ratio.

The combination of capillary forces and drying effects were also observed by Wang *et al.*¹³⁷ They compared two types of scCO₂ injection process, the first one with wet scCO₂ (WscCO₂, 100 % water saturated) and the second one with dry scCO₂ (DscCO₂, 0% water saturation), both at different flow rates, in a micromodel initially filled with water. The results showed a higher DscCO₂ sweep efficiency with saturations reaching values up to 3.3 times larger than for WscCO₂ saturations. From their high injection rates range they found three mechanisms that control the DscCO₂ displacements at pore scale:

- a capillary fingering at low injection rates,
- a cross over from capillary to viscous fingering at medium injection rate,
- viscous fingering at high injection rates.

The WscCO₂ displacements were controlled only by the first two mechanisms.

Furthermore, Wang *et al.*¹³⁷ also showed that the mutual solubility between scCO₂ and water changed dramatically the specific interfacial area, which doubled or tripled during the capillary fingering process. The drying effect therefore enhances the scCO₂ displacement efficiency by altering the "capillary pressure lock".

Displacement and dissolution combination. Buchgraber *et al.*⁴⁴ emphasized a new type of displacement pattern, namely a combination between dissolution of CO₂ in water and the displacement itself. This phenomenon involved three steps: a disconnection and displacement of the gas by snap off mechanisms, a shrinkage of CO₂ bubbles and then the complete dissolution of the gas phase. They also observed the effect of the capillary number (related to the flow velocity) on the size of the capillary trapped CO₂ bubbles. The lower the injection velocity, the larger amount of non-wetting phase is trapped by capillary effects. They were able to show heterogeneous and homogeneous dissolution of CO₂ in water, an interesting aspect for the study of the dissolution trapping, which is discussed in the next section.

Overall, the investigations of fluid flows in porous media have been conducted for years using micromodels, considering different situations for the injection methodology, the flowrates or the p, T conditions. The effect of several characteristics of the porous medium have been studied including the wettability, the geometry, etc. These experiments have allowed to define adimensional numbers, which can be used to characterize the CO₂ drainage and brine displacement (C_a , viscous ratio between the phase), leading to preliminary guesses towards increasing injectivity efficiency for the capillary trapping improvement. Although a growing number of experiments are now conducted in realistic pressure and temperature conditions, accounting for the different phase of CO₂ (*i.e.* liquid, gas or supercritical) in multiphase flows, further works are still required to finely determine those effects depending on the physical characteristics of the considered underground storage location. Indeed, pressure, temperature or salinity conditions are increasingly important for the determination of thermodynamic equilibrium, which drive both phase solubility. High pressure micromodels can equally be used to investigate these properties, as discussed in the next section.

4.2. Solubility of CO₂ in water and brine: Solubility trapping

Dissolution trapping is a key trapping mechanism for the long term safety of the CGS process. This phenomenon occurs directly beneath the whole scCO₂ plume, helped by the convection due to the fluids density difference¹⁵¹⁻¹⁵⁶ or within scCO₂ plumes by local phase partitioning.¹⁵⁷⁻¹⁵⁹ Chang *et al.* studied these local scCO₂ dissolutions, focusing on a non-equilibrium dissolution,¹⁰⁰ recently underlined with core-scale and field experiments.^{142, 143, 160-162} A 2D heterogeneous micromodel was used to give evidence and imaging showing this non-equilibrium dissolution. In the whole network, the dissolution process depended on the characteristics of water imbibing pathways, such as their number or their flow rate. Indeed, an increase in the number of water paths led to a faster

depletion of scCO₂ by dissolution; as well as a low velocity for the water flow, the concentration of sCO₂ reaching the solubility for very low velocity. The importance of the surface area is also a key factor. A higher contact area increases the mass transfer between the two phases and thus accelerates the depletion in sCO₂ by dissolution.

The diffusivity is also a key factor which contributes to solubility and mineral trapping. Even if there are many data on the diffusion coefficient of CO₂ in pure water at atmospheric pressure,^{163, 164} the high pressure microfluidic approach completes this knowledge by adding the salinity and pressure issues. Thus, the salinity, changing the property of the CO₂ phase, like solubility of CO₂ or dissociation constant,^{113, 165, 166} influences the diffusivity of CO₂ in geological reservoirs. The microfluidic approach competes with the time consuming method of PVT (Pulsed Video Thermography),¹⁶⁷⁻¹⁶⁹ as reported in Sell *et al.*¹⁷⁰ Indeed, they used a microfluidic platform combined with the fluorescein quenching depending on the pH, displaying the diffusion of CO₂ (**Fig. 16(a)**).¹⁷¹ They discovered that the diffusion coefficient was not influenced by the pressure, but it decreased when the salinity (the concentration in NaCl) increased (**Fig. 16(b)-(c)**). According to the study of Liu *et al.*⁵³ based on Raman spectroscopy, the solubility of CO₂ in brine (NaCl solution) also decreases when the salinity and the temperature increase (**Fig. 16(d)-(e)**). The microfluidic platforms allow fast processes such as CO₂ solubilization and diffusivity of CO₂ in water or brine. Some studies took advantages of this skill to follow the CO₂ solubility behavior with temperature variations,¹⁷² confirming the fact that the solubility of CO₂ in water decreases when the temperature increases.^{5, 173} Abolhasani *et al.*¹⁷⁴ developed a smart microfluidic platform for measuring the solubility of CO₂ in different solvents by monitoring the evolution of CO₂ bubbles over time using segmented microflows. The data were calculated from the reduction of volume between the initial and the final CO₂ plug. Cubaud *et al.*¹⁷⁵ also used a similar strategy based on segmented flows of CO₂ and water to study their mutual solubility and had identified three regimes: saturating, coalescing and dissolving regime.

During injection of scCO₂, water dissolves in scCO₂ stream and this phenomenon of drying dramatically affects the displacement process. Wang *et al.*¹³⁷ showed the impact of mutual solubility of scCO₂ and water and the fact that a scCO₂ is able to carry a great amount of water, enhancing the drainage of water by the scCO₂. They highlight that the injection model has to take into account:

- the change of rock properties with dry and wet scCO₂
- building models integrating the dry-out effects.

Rufai *et al.*⁶⁸ confirmed the importance of the drying phenomena with a study of NaCl brine evaporation with air and CO₂. They highlighted a nonlinear evaporation rate, mainly due to the deposition of salts that acted as a physical barrier to hydraulic connectivity.

The influence of the physical conditions on the drying mechanisms has been studied by Chang *et al.*¹⁷⁶ they showed the domination of water dissolution into scCO₂ for the depletion of residual CO₂ during imbibition experiments. The microfluidic

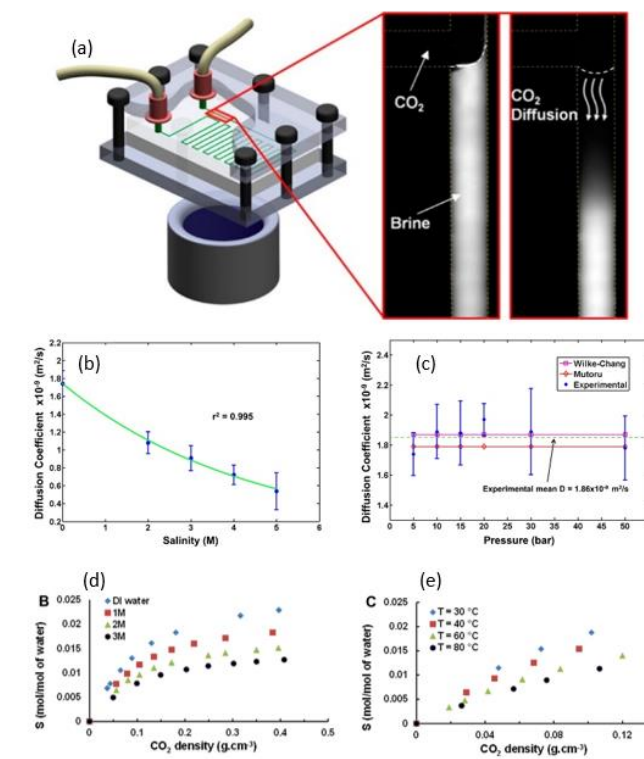


Fig. 16 (a) Scheme of the experimental setup used by Sell *et al.* to access to the diffusivity of CO₂ in brine. Images show the fluorescent quenching as CO₂ diffuses in brine (and acidifies the solution). (b) Diffusion coefficient in function of the salinity of the brine. (c) CO₂-brine diffusion depending of the pressure and the comparison with models provided by Wilke-Chang and Motoru,¹⁷⁰ (Reprinted with permission from Sell A., Fadaei H., Kim M., Sinton D. Measurement of CO₂ diffusivity for carbon sequestration: a microfluidic approach for reservoir-specific analysis. Environmental Science and Technology 2013, vol. 47, n°1, p. 71-78. Copyright (2020) American Chemical Society). (d) Solubility of CO₂ in brine found by Raman spectroscopy. The solubility decreases with the increase of the salinity. (e) Influence of the temperature on the solubility. A higher temperature induces a lower solubility, adapted from Liu *et al.* (2012)⁵³.

approach also promotes the study of factors influencing the CO₂ dissolution, like the addition of Nickel Nanoparticles (Ni NPs) into the CO₂ stream and the pH of the brine. With this technique, it has been proved that an addition of 30 mg·L⁻¹ Ni NPs increased the dissolution of CO₂ into the brine, especially with an acidic brine.¹⁷⁷

When a geological formation is subjected to depressurization, exsolution of CO₂ from the CO₂-saturated brine can occur.^{47, 128, 178-181} This phenomenon was also observed in the case of micromodels experiments¹⁸² (Fig. 17(a)). It was seen that the first step of instantaneous nucleation, after an oversaturation stage, is followed by the increase of number of bubbles as the pressure is decreasing. A strong capillary trapping is demonstrated by the correlation between bubbles and pore sizes distribution. Although the nucleation site for the bubble formation showed a random distribution, Xu *et al.*¹⁸² observed two types of preferential morphologies for the growth of CO₂ bubbles. The first one corresponds to a nucleation at the pore wall of a pore bodies, leading to a growth along a direction normal to the pore wall. The second involves a nucleation at the pore wall of a pore throat, leading to a growth into the adjacent pore body (Fig. 17(b)). In this study, an Ostwald ripening effect has also been observed for an exsolution at 25°C, but not at a temperature of 40°C.

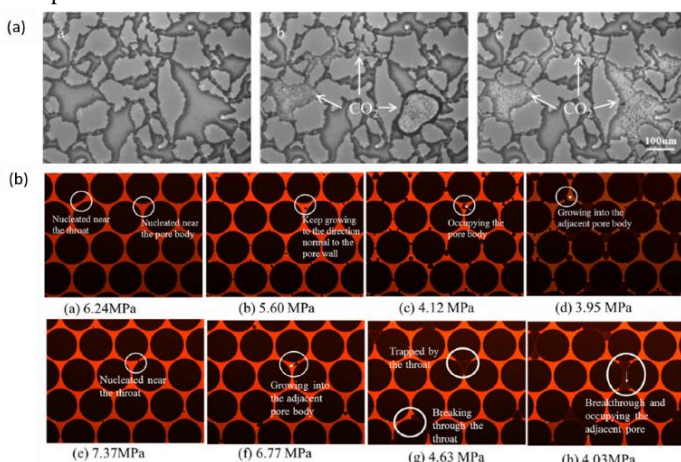


Fig. 17 (a) CO₂ exsolution from carbonated water (3.1 MPa).⁴⁷ (Reprinted with permission from Zuo L., Zhang C., Falta R. W., Benson S. M. Micromodel investigations of CO₂ exsolution form carbonated water in sedimentary rocks Advances in Water Resources 2013, vol. 53, p. 188-197. Copyright (2020) Elsevier). (b) (Color online) Growth of CO₂ bubbles in experiment Case 1 and 2. (a)–(d) correspond to case 1 ($T = 25\text{ }^{\circ}\text{C}$, $r_p = 5.13\text{ MPa/h}$). (e)–(h) correspond to case 2 ($T = 40\text{ }^{\circ}\text{C}$, $r_p = 5.13\text{ MPa/h}$).¹⁸² (Reprinted with permission from Xu R., Li R., Huang F., Jiang P. Pore-scale visualization on a depressurization induced CO₂ exsolution. Science Bulletin 2017, vol. 62, n°11, p. 795-803. Copyright (2020) Elsevier)

In brief, the main interest of high pressure micromodels approaches compared to conventional core-scale or field scale approaches for accessing data on the solubility trapping is the fast screening ability of such methodologies. By combining optical access – and therefore *in situ* characterization – with pressure and temperature capability and small scales, phase equilibrium can be reached in short times, while the space of investigation for the phase diagram is increased. Meanwhile, complex geometries can also provide means for salt precipitation kinetics determination (drying mechanism), depending on mass transfer at the pore scale through both diffusion and convection effects, which are experimentally difficult to access using core-flood experiments. The recent development of reactive micromodels allows for studying another critical aspect of CO₂

storage at the pore-scale, namely reactive fluids flows in porous media, which are discussed hereafter.

4.3. Materials dissolution / precipitation: Mineral trapping

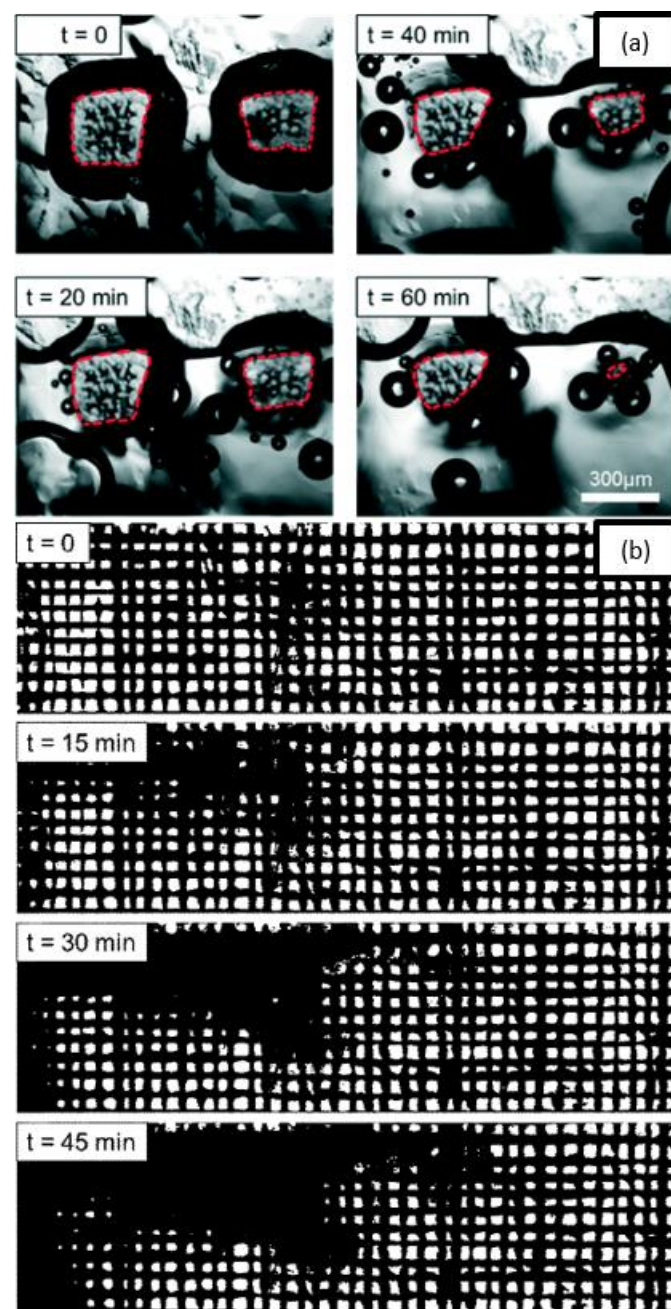


Fig. 18 (a) Preferential calcite dissolution through specific isotropic edges (b) phenomenon of wormholing (conduit formation).⁵⁸ (Reprinted with permission from Song W., de Haas T. W., Fadaei H., Sinton D. Chip-off-the-old-rock: the study of reservoir-relevant geological processes with real-rock micromodels. Lab on Chip, 2014, vol. 14, p. 4382-4390. Copyright (2020) The Royal Society of Chemistry.).

Material dissolution. The dissolution of CO₂ into a brine-saturated reservoir leads to an acidification of the flow, and it impacts carbonate minerals.¹⁸³⁻¹⁸⁵ In order to visualize the influence of this acidification on the carbonate reservoirs,

already reported at macro-scale,¹⁸⁶⁻¹⁸⁹ it is possible to mimic this phenomenon by flushing an acidified brine into a carbonate micromodel. For this purpose, Song *et al.*⁵⁸ injected a 1% HCl 1.81M NaCl brine through a natural calcite chip, with a straight channel or a two-dimensional micromodel. The direct visualization into a single microchannel permitted to visualize the carbonate-acid reaction producing CO₂ gas and to assess dissolution rates. The study in two-dimensional micromodel showed preferential calcite dissolutions depending on the crystal orientation and the local flow velocities, causing a phenomenon of wormholing (**Fig. 18**).

Minerals precipitation and crystallizations. The brine evaporation, even with non-reactive gases, leads to the precipitation of minerals. The microfluidics technology allows to more easily and more precisely study the sensitivity of governing parameters such as salinity, injection flow rate, capillary pressure, aqueous phase mobility and temperature¹⁹⁰ (in comparison with field or core-scale experiments).

For instance, an evaporation of NaCl brine in a water-wet micromodel showed permeability damages, due to NaCl crystallization. The impact on the permeability was dependent on the initial brine concentration.²⁴ The permeability alteration decreased with an increase of the brine concentration. Kim *et al.*²⁴ coupled the ability to follow the pH quenching of fluorescein due to CO₂ dissolution in water and the visualization of precipitation. They used a NaCl solution to mimic the aquifer brine and flushed a brined-filled “aquifers on a chip” micromodel with CO₂ gas.

The experiments with a single channel, including isolated pores, showed the formation of two different morphologies of precipitates, namely large bulk crystals and aggregated polycrystalline structures.⁶⁸ The large bulk crystals were formed away from the CO₂ flux whereas the aggregated polycrystalline structures appeared preferentially near the CO₂/brine interface (**Fig. 19(a)**). When the CO₂ was injected in a brine-filled regular-grid network, the porosity dramatically decreased after salts precipitation (between 15 and 20%) and the salts blockages occurred preferentially in the channels and less frequently at the channels intersections. The precipitation process followed the direction of the CO₂ flushing, and occurred fast. Before the first mineral precipitation, the authors found evidences of phase redistributions and initial brine evaporation (confirmed by the formation of dendritic-like structures, witnessing a sur-saturation process¹⁹¹), and then, the salt precipitation showed a linear rate. The micromodels allow the direct visualization of the propagation of the drying front, due to the pathways of the dry CO₂ into a NaCl brine.⁵⁰ As developed in the capillary trapping section, the formation of brine films on the rock surfaces and obviously along the CO₂ pathways, impacts the salt precipitation (rates, localizations, morphologies). The affinity of water with salts and rocks being strong, the salt precipitation occurs in the CO₂ stream, supported by brine transport along the mineral surface (water films conductivity) (**Fig. 19(b)**).

The effect of diffusivity and advection provided by the flow regime of fluids cannot be studied in batch.¹⁹²⁻¹⁹⁶ Zhang *et al.*¹⁰² completed macroscale experiments by mixing two aqueous phase of calcium and carbonate, respectively, into a microchip,

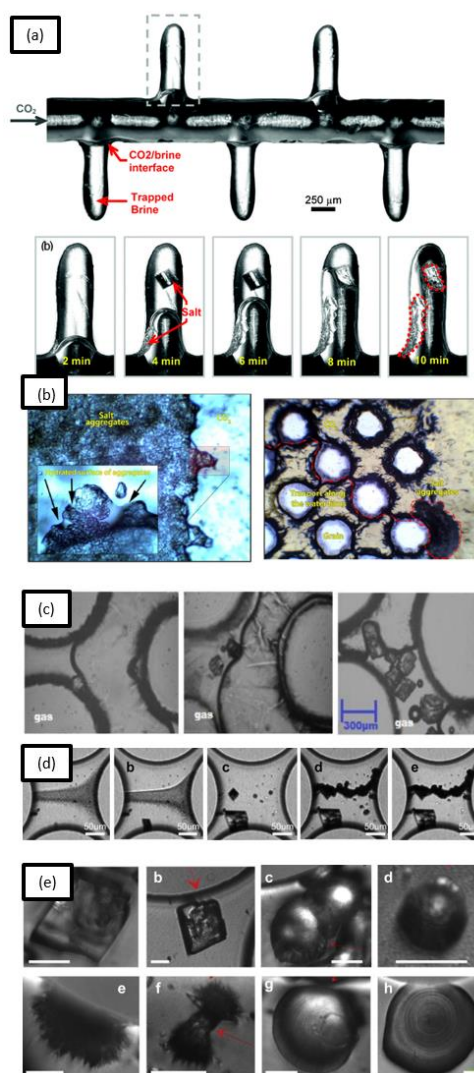


Fig. 19 (a) Salt precipitation during CO₂ injection. This experiment highlights two different morphologies precipitates: a large bulk crystal, forming away from the CO₂ flow, and an aggregate polycrystalline structure, developed at the interface between the brine and the CO₂.²⁴ (Reprinted with permission from Kim M., Sell A., Sinton D. Aquifer-on-a-Chip: understanding pore-scale salt precipitation dynamics during CO₂ sequestration. *Lab on Chip* 2013, vol. 13, n°13, p. 2508-2518. Copyright (2020) The Royal Society of Chemistry). (b) This image shows a magnified portion of a salt aggregate. The close-up shows that the surface of the aggregate is hydrated with a layer of water indicating high affinity of salt towards the water. Pore-scale visualization of aggregate growth in the homogenous micro-chip. Aggregates are supported with the transport of water through the capillary continuous water films. The images show that even very thin liquid bridges have a significant hydraulic conductivity.⁵⁰ (Reprinted with permission from Miri R., Noort R. V., Aagaard P., Hellevang H. New insights on the physics of salt precipitation during injection of CO₂ into saline aquifers. *International Journal of Greenhouse Gas Control* 2015, vol. 43, p. 10-21. Copyright (2020) Elsevier). (c) Mineral dissolution and regrowth observed in a single pore during an experiment without Mg.²⁰¹ (Reprinted with permission from Jaho S., Athanasakou G. D., Sygouni V., Lioliou M. G., Koutsoukos P. G., Paraskeva C. A. Experimental investigation of calcium carbonate precipitation and crystal growth in one- and two-dimensional porous media. *Crystal Growth and Design* 2016, vol. 16, n°1, p. 359-370. Copyright (2020) American Chemical Society). (d) Evolution of calcite (top) from blocky and dogtooth (size: 10-80 μm) to anhedral spheroidal (size 5-30 μm) and aragonite (bottom) from shrubs and fuzzy dumbbells (size: 5-60 μm) to spheroidal (size: 20-200 μm) (e) Salt precipitation at the interface of liquid and gas, gas released from the solution.⁴³ (Reprinted with permission from Boyd V., Yoon H., Zhang C., Oostrom M., Hess N., Fouke B., Valocchi A. J., Werth C. J. Influence of Mg²⁺ on CaCO₃ precipitation during subsurface reactive transport in a homogeneous silicon-etched pore network. *Geochimica et Cosmica Acta* 2014, vol. 135, p. 321-335. Copyright (2020) Elsevier).

confirming a precipitation along the center mixing line, as also reported elsewhere.^{77, 197} The microsystem experiments permitted the direct visualization of the porosity decrease (and thus the permeability reduction) induced by CaCO₃ precipitation. Concerning the morphologies, the Raman spectroscopy highlighted the formation of vaterite and calcite crystals. The whole experiment allowed the possibility to calculate the precipitation rates for each type of crystal and showed their dependence with the initial saturation state. The relative amount of the vaterite increased with the saturation state, as the quantity of precipitates decreased. The addition of Mg²⁺ to the initial mixture of CaCl₂ was studied in the same micromodel.⁴³ Indeed, Mg²⁺ is known to be an inhibitor in calcite formation.¹⁹⁸⁻²⁰⁰ The three CaCO₃ polymorphs were observed, calcite, vaterite and aragonite. The calcite polymorph was the most abundant in all experiments and the amount of the aragonite polymorph increased with the concentration of Mg²⁺. The morphology of calcite varied depending on the Mg²⁺ concentration, changing from angular forms to spherical (needle like to spherical for aragonite, with an increase of crystal size) (**Fig. 19(c)**). At a higher level, the presence of Mg²⁺ strongly affected the porosity, the permeability of the porous media and the wideness of the downstream precipitation area, due to a delayed precipitation. A phenomenon of dissolution of small crystals and regrowth in bigger polymorphs was observed (**Fig. 19(d)**).

Jaho *et al.* performed some experiments with oversaturated solution of CaCl₂·2H₂O and NaHCO₃, reacting in a 2D micromodel.²⁰¹ They observed preferential area for the precipitation reaction, namely close to the inlet and even closer when the saturation ratio value increased. A change in temperature led to different carbonate precipitation rates and thus influenced the drop of porosity observed during the experiment.²⁰² The direct microscale observation permitted to visualize formation of CaCO₃ at the interface between gas and liquid (**Fig. 19(e)**). A gas phase was produced during the experiment when the temperature was increased. They made the hypothesis that the gas bubbles surface should act like a heterogeneous nucleation catalyst due to the high surface energy (induced by the smallness of the bubbles).

Effects of flow rate and CO₂ phase on precipitation. Nooraeipour *et al.*²⁰³ studied an evaporation regime drying brine into a matrix of shale micromodel. They observed two distinct forms of crystals: (a) large and semi-large (100 – 300 µm) single cubic crystals of halite (in the aqueous phase) and (b) dense micrometer-sized (< 20µm) halite crystals (on the interface of rock and CO₂ stream). They linked the formation of each one to different structures of residual brine (domes, pools, films). The distribution of the different brine dispositions changed with the temperature and the flow rates, such as the appearance of each kind of crystals. They also highlighted that the phase of CO₂ changed the relative amount of crystals.

The large amount of salt transport and precipitation experimental studies in porous media at the pore scale in recent years has also generated data that can be incorporated into numerical models in order to predict salt precipitation patterns.²⁰³⁻²⁰⁷

Finally, geological micromodels integrating or mimicking mineralogy have been used to provide new insights for

investigating the mineral trapping of CO₂ in a CGS process. The complementarity between pore-scale investigations with optical access and core-scale experiments has been highlighted. Undeniably, the last technological developments have demonstrated the possibility to perform experiments directly on real geological materials, at pore-scale and with a direct visualization. The fast screening capability opens ways to separately investigate the coupled mechanisms and the geochemical reactions. This also permits to quickly identify the critical geochemical processes that are affected by the geometry and the topology and to get an idea about the strength of this synergy. As physical and chemical phenomena can lead to different crystal morphologies or precipitation rate, it is important to account for the deep biosphere in each specific reservoir. Indeed, this can strongly impact the local chemical environment due biological mechanisms involving the metabolisms of indigenous microorganisms. Hence, the issue of bio-geo-chemical impacts in CGS processes and how the micromodel investigations deal with the integration of underground biological material are discussed in the following section.

4.4. Biogeochemical effects

Underground microorganisms have severe impacts on deep subterranean processes when *in situ* conditions allow life (temperature, porosity, permeability...). After a large study summarizing all the results from a hundred sites, Magnobosco *et al.*²⁰⁸ estimated that the biomass of this intraterrestrial life would be between 23 and 31 Gt of carbon. These values have been significantly reduced if we compare them to previous works on the subject.²⁰⁹⁻²¹¹ They remain, nevertheless, very important since the mass of carbon of all these microorganisms would be 245 to 385 times higher than the mass of carbon represented by the whole humanity. These intraterrestrial microorganisms can modify the microporous network through three main mechanisms: (i) the modification of the mineral surface properties leading to wettability alteration within the porous structures^{212, 213}; (ii) the microsystem bioclogging with biomass accumulation, contributing to a decrease in permeability^{214, 215} and combined modification of the mineral surface properties, the geochemistry, and the overall hydrodynamic of the porous media²¹⁶; and (iii) the precipitation biominerals, mainly carbonates, causing also clogging in the porous network.²¹⁷⁻²¹⁹ It has also been demonstrated at the Ketzin geological storage site (CO₂SINK project) that the metabolic activity of the sulfate-reducing microorganisms clogged the porosity of the aquifer nearby the well Ktzi 201 because of the sulfide generated combining with dissolved iron to form iron sulfides.²²⁰

Sequestered CO₂ can also have a great impact on microbial activity (directly into the aquifer or in potable groundwater after a leak).²²¹⁻²²³ It is known that high pressure and high temperature CO₂ concentration can lead to cell inactivation.^{224, 225} In spite of this aspect, some studies discovered that the growth of biofilms, complex three dimensional structures of bacteria communities, can result in permeability reduction (bioclogging) and secure CO₂ sequestration processes.²²⁶⁻²²⁸

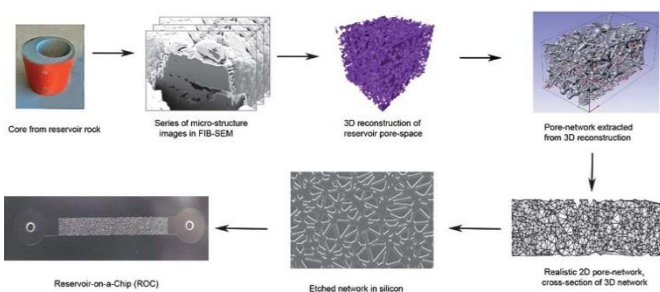


Fig. 20 The conceptual flow-map for ‘Reservoir-on-a-Chip’⁶¹ (Reprinted with permission from Gunda N. S., Bera B., Karadimitriou N. K., Mitra K. S., Hassanizadeh M. Reservoir-on-a-Chip (ROC): a new paradigm in reservoir engineering. *Lab on Chip* 2011, vol. 11, n°22, p. 3785-3792. Copyright (2020) The Royal Society of Chemistry).

Sygouni *et al.* studied the impact of CO₂ on *Pseudomonas putida* biofilms in a glass-etched porous media.²²⁹ The cells were diluted in nutrient broth at a concentration between 10⁷ and 10⁸ cfu·mL⁻¹ and introduced in a glass/glass pore network.²³⁰ The pH before the injection was 7.1. They observed that the CO₂ injection has only a temporarily effect on the biofilms. Indeed, as the CO₂ injections reduce the pH, causing cell stress, and a partially detachment of the *P. putida* biofilm, regrowth was observed. The CO₂ concentration in the porous media was then reduced by the nutrient flow reimbibing the porous media and some buffering reactions consuming CO₂. They also observed that the biofilms age is a key factor for biofilm resistance to the CO₂ injection. Actually, older biofilms are denser and more resistant to breakdown during CO₂ injection. This study confirmed also the impact of the biofilm on the relative permeability of the porous media, and showed that the initial low permeability (due to the presence of the bacteria film) is quickly reached.

The micromodel can also be used to directly see the porosity decrease due to biomineralization, already shown at higher scale.^{218, 231-233} In a further stage, the study of Singh *et al.*¹¹⁶ also showed that an active metabolism is needed to have a CaCO₃ “bio-precipitation”, activated by the presence of NO₃⁻. The ability to couple the experiments with Raman spectroscopy provides information about CaCO₃ crystal morphologies (dendritic and lumped-type), identified as calcite and vaterite. As noticed for experiments with transverse mixing of CaCl₂ and Na₂CO₃ solutions, CaCO₃ biomineralization displays also a biofilm formation along a centerline, but a wider zone for the biofilm and the biomineralization process. An interesting use of fluorescent tracers and Elemental Scanning Electron Microscopy (ESEM) imaging showed that CaCO₃ precipitates occupied the whole depth of the pore and will thus strongly affect the porosity of the sub-surface formation, decrease the permeability of the geological reservoir and increase the complexity of the flow pathways of the injected fluid.¹¹⁶

The development prospects of high-pressure micromodels applied to the microbiology of deep environments go far beyond the context of the geological storage of CO₂. For instance, MEOR technologies aim to improve the recovery of underground crude oil using microorganism’s metabolites (*e.g.* biosurfactants, biopolymers, acids, solvents and gases).²³⁴ Micromodels are already useful tools to investigate and

understand classical EOR processes in reservoir conditions. Lifton reviewed the large microfluidic approaches usage in the EOR field.²³⁵ An outstanding microfluidic instrument for EOR investigations is the “Reservoir-On-a-Chip” (ROC) device (Fig. 20), first introduced by Gunda *et al.* to study realistic pore-network waterflooding in oil-bearing reservoir rock.⁶¹ Actually, by using the ROC device, He *et al* were able to visualize the real-time surfactants performance on oil recovery within porous media conditions (*i.e.* pore sizes similar to shale formation rocks).²³⁶ The latest developments among the microfluidic approaches include the study of the combined application of CO₂ storage and oil recovery processes.²³⁷⁻²³⁹

Understand microbial behavior deep underground gives insights to the bioplugging mechanisms leading to significant changes within the porous media, such as the reduction of the porosity and the permeability.^{240, 241} Engineering bioplugging has been used for several industrial applications (*e.g.* microbial enhanced oil recovery - MEOR, bioremediation). However, only few studies have investigated these phenomena at pore scale. Karembeigi *et al.*²⁴¹ used micromodels to look at the potential of bioplugging to increase the water flooding efficiency in high permeable zones. Liu *et al.*²¹⁶ studied the hydrodynamic effects on biofilm growth and detachment with a T-shape microchannel (Fig. 21). These studies bring significant understanding in the bioplugging effects at pore scale for various underground processes such as MEOR.

The bio-agents produced in MEOR have the same properties as conventional surfactants but offer a better substitute thanks to their lower operating cost, lower toxicity, and higher

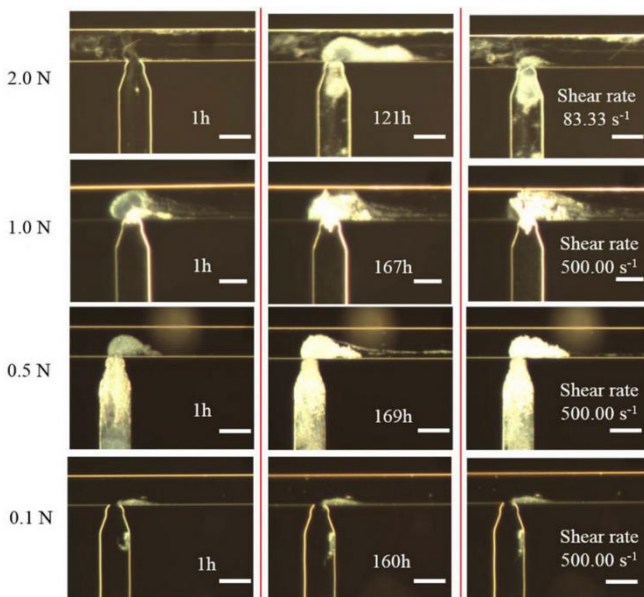


Fig. 21 Optical images of biofilm growth over time at various nutrient concentrations, 2.0 N, 1.0 N, 0.5 N, and 0.1 N, respectively. Images in the left column were taken after injecting nutrients for 1 h. The middle column shows images of biofilm growth for around 7 days. The right column lists images of biofilm detachment by increasing shear rate to 500.00 s⁻¹. Nutrients flow from right to left in the upper channel. Scale bars indicate 100 µm.²¹⁶ (Reprinted with permission from Na L, Skauge T., Landa-Marban D., Hovland B., Thorbjørnsen B., Radu F. A., Florkzyk B. Microfluidic study effects of flow velocity and nutrient concentration on biofilm accumulation and adhesive strength in the flowing and no-flowing microchannels. *Journal of Industrial Microbiology and Biotechnology* 2019, vol. 46, n°6, p. 855-868. Copyright (2020) SpringerNature).

biodegradability^{242, 243}. Several field and laboratory investigations have been carried out using *in situ* and *ex situ* biosurfactant flooding tests (*i.e.* use of naturally occurring surfactant-producing microbes or injection of surfactant-producing microorganisms into the reservoirs, and injection of biosurfactant fluid into the reservoirs, respectively) to study their dispersive effects on EOR by altering the surface tension, interfacial tension and wettability^{234, 244}. Despite their promising properties and attractive alternative compared to chemical surfactants, and because of a lack of knowledge of microbial consortia mechanisms and biosurfactant interactions with reservoirs geochemistry, MEOR technologies are not considered yet as a viable process by the oil industry^{242, 243}. In the MEOR context, micromodels (*e.g.* GLoCs) are an excellent tool to study and understand the crude oil dispersion by biosurfactant flow mechanisms within reservoir conditions (*i.e.* pore scale, high pressure and high temperature). Indeed, Soudmand-Sali *et al.* designed both fractured and non-fractured etched-glass micromodels with irregular and dead-pore network patterns to study the *in situ* MEOR effects with *Bacillus subtilis*, which produces surfactin as a biosurfactant, on oil recovery efficiency and wettability alteration according to fracture orientation in porous media. They observed no sign of wettability alteration during the *in situ* MEOR process and because of the efficient surfactin decreasing effect on the interfacial tension and viscosity, combined to better oil-fluid miscibility, they obtained higher oil recovery efficiency within the fractured models compared to the non-fractured one²¹². Within one of the same 2D patterned micromodels, Amani *et al.* analyzed *ex situ* MEOR process to investigate the effect of a rhamnolipid mixture, a biosurfactant produced by a model strain *Pseudomonas aeruginosa* (HATH), on oil recovery efficiency. The tested biosurfactant provided effective results on both oil emulsion and dispersion and displayed good stability over a wide range of temperatures, pH and different salt concentrations²⁴⁵. Interestingly, Armstrong & Wildenschild²⁴⁶ studied both *ex situ* and *in situ* MEOR with the microbial strain *Bacillus mojavensis* that produces biosurfactant and causes bioclogging. They demonstrated a better oil recovery when biosurfactant and bioclogging were occurring simultaneously, assuming that the microbial biofilm changed the pore morphology and allowed to re-direct the flow through preferential paths (Fig. 22). Those studies demonstrate successful oil recovery processes within porous media and provide good MEOR candidates for both *in situ* and *ex situ* MEOR industrial applications.

If pressure is a driving parameter within deep subsurface reservoirs^{247, 248} to take into account for underground processes investigations, most of the studies are done at atmospheric pressure. Recent investigations determine the effect of elevated pressure on these phenomena but barely use porous media to reproduce the reservoir porosity.²³²

As a matter of fact, several studies have already reported the major key role of subsurface microbial communities (*i.e.* the deep biosphere) in deep bio-geochemical cycles^{208, 249}. The microorganisms' metabolisms have been proven to greatly impact the local biogeochemical environment, in particular in the case of CGS or MEOR. These effects have been mostly studied

using modeling approaches to simulate the CO₂ injection effects on indigenous deep reservoir communities^{250, 251} and on the combined MEOR-CO₂ injection process^{139, 252}, but still require raw data obtained experimentally at small scales. In this view, micromodels present several interests to gain better understanding of the underground geo-microbiology at small scale, being able to reproduce in particular the local mineralogy and porosity into which biofilms can form. Such tools are particularly well adapted to investigate the common effects of flow, geochemistry and geobiology occurring at various location of a deep reservoir. The particular case of microorganisms' transport in porous media and the further biosurfactant generation (modifying the local interfacial tensions and capillary numbers) and biomineralization process of CO₂ have been studied, taking advantage of the design flexibility of the micromodels. GLoCs devices represent a more realistic approach, at lab scale, to increase our understanding of the mutual influence of microbes on the geochemistry and vice versa, and to better estimate the strong relationship between the fate of scCO₂ in the storage aquifers and the endemic microbial communities.

5. Challenges and Opportunities

Investigating CO₂ geological storage at the pore scale can provide a significant amount of information for feeding numerical modeling approaches and understanding the involved phenomena. Despite the numerous proofs of concept that have been demonstrated so far, several challenges remain, which could open new opportunities for the technology of Geological Labs on a Chip (GLoCs) in relation with deep underground problematics.

The link between lab and field. CO₂ geological storage is a promising technology for the management of CO₂ anthropogenic

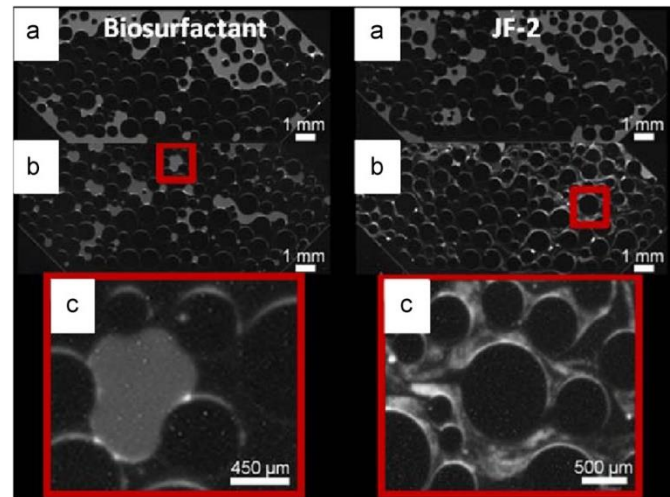


Fig. 22 Biosurfactant flood (left) and JF-2 flood (right); (a) primary recovery, (b) residual oil saturation after enhanced recovery. Red box in (b) corresponds to enlarged region in (c). JF-2 biofilm can be seen in the right-hand column as dense streamlined gray matter (b) and (c)²⁴⁶ (Reprinted with permission from Armstrong R. T., Wildenschild D. Investigating the pore-scale mechanisms of microbial enhanced oil recovery. Journal of Petroleum Science and Engineering 2012, vol. 94-95, p. 155-164. Copyright (2020) Elsevier).

emissions. Although the equipment for large-scale geological storage is capital intensive, major challenges that will also create technological opportunities are the economic drivers, including legislation, that will make the capital investment viable. This includes a future with automated feedback between the micromodels experimentation in the laboratory and field operations, capable of exchanging real-time data and detailed understanding of the heterogeneity of the reservoir formations. In particular, the mineralogy can be complex, yet a fingerprint exclusive to each geological formation could be integrated in the micromodels technologies. Therefore, libraries of reservoir information should somehow be connected to the design of laboratory experiments.

Below the pore scale. The physical models applicable to microporous geological storage fall apart at the nano-scale, relevant to tight shale and the transport within crystalline lattices. Bridging the micro- to the nano-scale can be accomplished by using natural or synthetically prepared materials injected into microfluidic devices. However, further opportunity remains to design micro and nano-models that can capture molecular-scale information. This may include the development of nanofluidics devices^{253–255}, which have proven to be excellent tools for accessing critical phenomena at the molecular level, including non-conventional phase behaviors. However, challenges still need to be addressed in term of experimentation (clogging, non-validity of conventional fluid mechanics equations, etc.). This should also include the development and use of more advanced *in situ* characterization tools at such scales^{256, 257} and multi-scale modeling algorithms that rely on high-performance computing. Water chemistry itself is incredibly complex, yet central to understand CO₂ capture with GLoCs. *In situ* and in-time characterization and advanced computational methods that can decipher aqueous solutions structures/properties and how they interact with other phases to store CO₂, with high enough resolution to validate proposed mechanisms, are also tremendous opportunities.

Ultra high-pressure experiments. The current microfabrication technologies based on silicon-Pyrex allows investigating, at the lab scale, phenomena occurring in typical ranges of [-50°C – 400°C] and [0.1 MPa – 30 MPa]. However, it can be anticipated that a growing need to understand much higher pressure phenomena than that which cannot be currently studied at the pore scale. In particular, at some point, people may consider the injection of CO₂ into deeper and deeper subterranean reservoirs, and thus requiring ultra-high pressure experimental set-ups in the 350 – 1000 bar range (*i.e.* ~ 5,000–15,000 psi). Additionally, this could open several opportunities towards the investigation of other deep underground related studies such as geothermal energy storage or magma displacement studies. In this view, there will soon exist a strong need to innovate into a new field of ultra-high-pressure microfluidics, redesigning our current methods for device fabrication, operation, and laboratory safety.

Investigating deep life. Besides the studies of reactive fluid flows and geochemical-mechanical effects induced by CO₂ injection in deep underground, geomicrobiology can also benefit

from the latest developments in this field. Indeed, only few laboratories in the world are equipped to carry out microbiology under high pressure for technical and safety reasons. The study and the manipulation of these microorganisms under these conditions require the use of adapted equipment quite cumbersome. These pressurized devices can be ranged from one milliliter to several liters. These first reasons may already represent serious limitations to the study of microorganisms under elevated pressures.

These devices designed to withstand high pressures also do not allow the direct observation of phenomena at the microorganisms or the pore scales, which could provide information on the real-time microbial activity. Unfortunately, conventional experimental equipment is only able to do so if measurements are done by sub-sampling or at the end of the experiment after sacrificing the microbial culture. Sampling procedures are however very challenging due to the numerous changes occurring while the sample is depressurized (strong chemical changes due to the degassing of CO₂). Therefore, the use of high pressure micromodels is a possible response to overcome these different constraints, allowing the “democratization” of high pressure microbiology. By controlling the pattern of the micromodel, the pressure, the temperature, the composition of the culture medium, the microbial composition (axenic strain, simplified community or autochthonous community from a targeted environment), such microtools can simulate extreme environments and stimulate new multidisciplinary research based on optical and (multi-) spectroscopic analyses. Compared to post mortem examination obtained when opening an autoclave, it is expected that these approaches will provide new insights that are more realistic.

Reactive transport and couplings. The recent development of these new nano-micro-fluidic tools mimicking geological environments (Geological labs on a Chip – GLoCs) has opened new fields of research and allows fine characterization of the reactivity of porous geological media. Indeed, the GLoCs technology allows reconsidering couplings between different physical, chemical, mechanical and microbiological processes. The scientific community agrees on the fact that these phenomena need to be studied individually before their couplings and upscaling. The downscaling to the nano-metric or even molecular level is the right scale for investigating reactive processes and mass and heat transfers.

Significant advances have been made over the past 2 decades, in particular by trying to transcribe the reactive transport challenges with the associated scientific locks in order to conceptualize GLoCs experiments sufficiently simplified to study the kinetics of geochemical reactions, the interfacial properties, the effects of temperature and pressure and the flowing mechanisms (advection, convective, diffusive and capillary). This complexity is found in particular in heterogeneous flows, mineralogical distribution, mixtures between fluids having evolved differently thanks to chromatographic effects and the heterogeneity of the porous media. Thus, GLoCs will allow revisiting several scientific obstacles including:

- the role and the impact of preferential flows in a complex network of drains, whose pores and crossings create highly reactive mixing zones (far from thermodynamic equilibrium) in a hydrodynamically heterogeneous medium
- the acquisition of thermokinetic reactions data of minerals dissolution / precipitation in a saline context, in particular including the effects of common ions and migration / covering of meta-stability zones of mineral phases
- the identification of the reactive properties of highly capillarized multiphasic systems, including the role of the interfacial tensions, the wettability of the minerals and the contact angle under different flows and connection regimes of the porous network
- The identification of metastable and ephemeral redox species under catalysis of bacterial microorganisms in CO₂ storage systems (properties of biofilms, inhibition / catalysis of mineral surface processes, etc.)
- The understanding of small-scale geochemical/biogeochemical gradients formations and the effect of micro-environments on larger scales.
- The investigation of the coupling levels between different processes (flow, geochemical reactions mechanisms at phases interfaces, etc.)
- The use of geophysical techniques to characterize the electrokinetic and electrochemical properties of mineral phases and interfaces between wetting and non-wetting fluids, and their evolving
- The review of the theoretical approaches of reactive transport and the numerical coupling between processes (thermo-hydro-chemo-mechanical-biological) induced by the geological storage of CO₂ and the use of the subsoil for the energy transition.

Therefore, GLoCs offer great hope for capturing key processes at appropriate scales, which will make possible to perform downscaling and upscaling in order to capture the spatial and temporal footprints of different processes highlighted at "small scales: GLoCs" and their expression at "large scales: reactive column and near CO₂ injection well". Finally, the nano-micro-fluidics devices with optical and spectroscopic techniques allow characterization and monitoring of the evolution of the different phases under the geological subsoil conditions. The quantitative interpretation of these observations will allow re-evaluating/improving thermodynamic and kinetic parameters of the involved geobiochemical reactions related to the interfacial properties inducing mass exchanges. This will provide sufficiently generic and general knowledge on the reactive transport parameters (relative permeabilities, reactive surfaces, structural and mineralogical heterogeneities of the porous medium, wettability, fluid repartition in the porous network media, etc.).

Conclusions

High pressure micromodels (Geological Labs on a Chip – GLoCs) have already been demonstrated to be unique platforms for investigating CO₂ geological storage mechanisms at the pore scale. Indeed, they bring additional information compared to conventional batch or core-scale procedures and have been used

so far to investigate thermodynamics, hydrodynamics in porous media, geochemistry, geobiological effects, reactive flows or solubility and diffusivity measurements. They have yielded complex designs geometries – 2D, 3D, reactive or not – depending on the targeted information and have been already coupled to several *in situ* characterization techniques allowing understanding at the appropriate scales numerous phenomena (mass transfer, multi-phase flow in porous media, interfaces characterization, etc.). Further development towards nanoscale, along with the integration of adapted characterization techniques will provide additional information at the molecular level. Moreover, the ability to proceed with microfabrication technological developments should open new methods towards ultra-high pressure experimentation at small scales, which could be used for investigating very deep geological environment. Overall, the CGS related R&D activities are highly interdisciplinary since they are based on chemical engineering, (geo)chemistry, flow chemistry, geosciences, physics, hydrodynamics of multiphase flows, microbiology, etc. Therefore, high pressure micromodels are new experimental approaches to investigate the mechanisms involved in CGS processes at the pore scale, all relevant for chemical engineers, chemists or geoscientists, far beyond the sole CGS-related topics. Eventually, the expansion of such systems to microbiology could speed up the discovery of deep underground microbes, recently highlighted as the "unseen majority" of living organisms, which largely contribute to the general carbon cycles on Earth.

Conflicts of interest

The authors declare no conflicts of interest.

Acknowledgements

The authors acknowledge financial support from the National Research Agency (ANR) for the financial support of the project CGSμLab, reference: ANR-12-SEED-0001). This work has received funding from the European Research Council (ERC) under the European Union's Horizon 2020 research and innovation program (Grant Agreement No. 725100, project Big MAC). The authors are also really grateful to the CNES for financial support.

Notes and references

1. R. Jackson, C. Le Quéré, R. Andrew, J. Canadell, J. Korsbakken, Z. Liu, G. Peters and B. Zheng, *Environmental Research Letters*, 2018, **13**, 120401.
2. C. Le Quéré, R. M. Andrew, P. Friedlingstein, S. Sitch, J. Hauck, J. Pongratz, P. Pickers, J. I. Korsbakken, G. P. Peters and J. G. Canadell, *Earth System Science Data*, 2018, **10**, 2141-2194.
3. C. M. White, D. H. Smith, K. L. Jones, A. L. Goodman, S. A. Jikich, R. B. Lacount, S. B. Dubose, E. Ozdemir, B. I. Morsi and K. T. Schroeder, *Energy & Fuels*, 2005, **19**, 659-724.
4. V. Alvarado and E. Manrique, *Energies*, 2010, **3**, 1529-1575.

5. S. M. V. Gilfillan, B. S. Lollar, G. Holland, D. Blagburn, S. Stevens, M. Schoell, M. Cassidy, Z. Ding, Z. Zhou, G. Lacrampe-Couloume and C. J. Ballentine, *Nature*, 2009, **458**, 614-618.
6. N. Mac Dowell, P. S. Fennell, N. Shah and G. C. Maitland, *Nature Climate Change*, 2017, **7**, 243-249.
7. S. Budinis, S. Krevor, N. Mac Dowell, N. Brandon and A. Hawkes, *Energy Strategy Reviews*, 2018, **22**, 61-81.
8. S. Bachu, *Energy Conversion and Management*, 2002, **43**, 87-102.
9. T. Gleeson, K. M. Befus, S. Jasechko, E. Luijendijk and M. B. Cardenas, *Nature Geoscience*, 2016, **9**, 161-167.
10. R. T. Okwen, M. T. Stewart and J. a. Cunningham, *International Journal of Greenhouse Gas Control*, 2010, **4**, 102-107.
11. J.-P. Nicot, *International Journal of Greenhouse Gas Control*, 2008, **2**, 582-593.
12. L. Wallquist, V. H. M. Visschers and M. Siegrist, *Environmental Science and Technology*, 2010, **44**, 6557-6562.
13. F. M. Orr Jr., *Journal of Petroleum Technology*, 2004, **56**, 90-97.
14. S. Taku Ide, K. Jessen and F. M. Orr, *International Journal of Greenhouse Gas Control*, 2007, **1**, 481-491.
15. M. a. Hesse, F. M. Orr and H. a. Tchelapi, *Energy Procedia*, 2009, **1**, 3275-3281.
16. A. Kumar, M. Noh, G. A. Pope, K. Sepehrnoori, S. Bryant and L. W. Lake, *Society of Petroleum Engineers*, 2004, **89343**, 1-10.
17. M. Abolhasani, A. Günther and E. Kumacheva, *Angewandte Chemie International Edition*, 2014, **53**, 7992-8002.
18. S. G. R. Lefortier, P. J. Hamersma, A. Bardow and M. T. Kreutzer, *Lab on a Chip*, 2012, **12**, 3387-3391.
19. R. Sun and T. Cubaud, *Lab on a Chip*, 2011, **11**, 2924-2928.
20. I. Gaus, *International Journal of Greenhouse Gas Control*, 2010, **4**, 73-89.
21. B. M. Sass, N. Gupta, J. A. Ickes, M. H. Engelhard, D. R. Baer, P. Bergman and C. Byrer, "First National Conference on Carbon Sequestration, Washington, D.C., May 15-17", 2001.
22. R. Lenormand, C. Zarcone and A. Sarr, *Journal of Fluid Mechanics*, 1983, **135**, 337-353.
23. R. Lenormand and C. Zarcone, *Society of Petroleum Engineers*, 1984, **13264**, 1-17.
24. M. Kim, A. Sell and D. Sinton, *Lab on a chip*, 2013, **13**, 2508-2518.
25. S. Marre, A. Adamo, S. Basak, C. Aymonier and K. F. Jensen, *Industrial & Engineering Chemistry Research*, 2010, **49**, 11310-11320.
26. S. Marre, Y. Roig and C. Aymonier, *Journal of Supercritical Fluids*, 2012, **66**, 251-264.
27. C. Zhang, M. Oostrom, T. W. Wietsma, J. W. Grate and M. G. Warner, *Energy and Fuels*, 2011, **25**, 3493-3505.
28. A. Bielinski, PhD Thesis, University of Stuttgart, Stuttgart, Germany., 2007.
29. H. Darcy, *Les fontaines publiques de la ville de Dijon : Exposition et application des principes à suivre et des formules à employer dans les questions de distribution d'eau; ouvrage terminé par un appendice relatif aux fournitures d'eau de plusieurs villes au filtrage des eaux et à la fabrication des tuyaux de fonte, de plomb, de tole et de bitume*, V. Dalmont, Paris, 1856.
30. C. Cottin, H. Bodiguel and A. Colin, *Physical Review E - Statistical, Nonlinear, and Soft Matter Physics*, 2010, **82**.
31. P. G. de Gennes and E. Guyon, *J Mec*, 1978, **17**, 403-432.
32. E. W. Al-Shalabi and B. Ghosh, *Journal of Petroleum Exploration Production Technology*, 2018, **8**, 217-228.
33. S. Gogoi and S. B. Gogoi, *Journal of Petroleum Exploration Production Technology*, 2019, **9**, 2263-2277.
34. M. L. Hoefner and H. S. Fogler, *AIChE Journal*, 1988, **34**, 45-54.
35. M. Liu and P. Mostaghimi, *Chemical Engineering Science*, 2017, **173**, 121-130.
36. L. Luquot, O. Rodriguez and P. Gouze, *Transport in Porous Media*, 2014, **101**, 507-532.
37. H. Ott, K. d. Kloet, M. v. Bakel, F. Vos, A. v. Pelt, P. Legerstee, A. Bauer, K. Eide, A. v. d. Linden, S. Berg and A. Makurat, *Review of Scientific Instruments*, 2012, **83**, 084501.
38. A. Bandopadhyay, T. Le Borgne, Y. Méheust and M. Dentz, *Advances in Water Resources*, 2017, **100**, 78-95.
39. Q. Sheng and K. Thompson, *Water Resources Research*, 2013, **49**, 5973-5988.
40. A. Martin, S. Teychené, S. Camy and J. Aubin, *Microfluidics Nanofluidics*, 2016, **20**, 92.
41. N. K. Karadimitriou, M. Musterd, P. J. Kleingeld, M. T. Kreutzer, S. M. Hassanizadeh and V. Joekar-Niasar, *Water Resources Research*, 2013, **49**, 2056-2067.
42. T. Baumann and C. J. Werth, *Vadose Zone Journal*, 2004, **3**, 434-443.
43. V. Boyd, H. Yoon, C. Zhang, M. Oostrom, N. Hess, B. Fouke, A. J. Valocchi and C. J. Werth, *Geochimica et Cosmochimica Acta*, 2014, **135**, 321-335.
44. M. Buchgraber, A. R. Kovsek and L. M. Castanier, *Transport in Porous Media*, 2012, **95**, 647-668.
45. F. Kazemifar, G. Blois, D. C. Kyritsis and K. T. Christensen, *Water Resources Research*, 2015, **51**, 3017-3029.
46. S. Morais, N. Liu, A. Diouf, D. Bernard, C. Lecoutre, Y. Garrabos and S. Marre, *Lab on a Chip*, 2016, **16**, 3493-3502.
47. L. Zuo, C. Zhang, R. W. Falta and S. M. Benson, *Advances in Water Resources*, 2013, **53**, 188-197.
48. A. L. Harrison, G. M. Dipple, W. Song, I. M. Power, K. U. Mayer, A. Beinlich and D. Sinton, *Chemical Geology*, 2017, **463**, 1-11.
49. Y. Kim, J. Wan, T. J. Kneafsey and T. K. Tokunaga, *Environmental Science and Technology*, 2012, **46**, 4228-4235.
50. R. Miri, R. V. Noort, P. Aagaard and H. Hellevang, *International Journal of Greenhouse Gas Control*, 2015, **43**, 10-21.
51. C. Zhang, M. Oostrom, J. W. Grate, T. W. Wietsma and M. G. Warner, *Environmental Science and Technology*, 2011, **45**, 7581-7588.
52. Y. Wang, C. Zhang, N. Wei, M. Oostrom, T. W. Wietsma, X. Li and A. Bonneville, *Environmental Science and Technology*, 2013, **47**, 212-218.
53. N. Liu, C. Aymonier, C. Lecoutre, Y. Garrabos and S. Marre, *Chemical Physics Letters*, 2012, **551**, 139-143.
54. C. Chang, T. J. Kneafsey, Q. Zhou, M. Oostrom and Y. Ju, *International Journal of Greenhouse Gas Control*, 2019, **86**, 11-21.
55. C. Chalbaud, M. Robin, J.-M. Lombard, F. Martin, P. Eggermann and H. Bertin, *Advances in Water Resources*, 2009, **32**, 98-109.

56. S. C. Cao, S. Dai and J. Jung, *International Journal of Greenhouse Gas Control*, 2016, **44**, 104-114.
57. M. L. Porter, J. Jiménez-martínez, R. Martinez, Q. McCulloch, J. William and H. S. Viswanathan, *Lab on a Chip*, 2015, **15**, 4044-4053.
58. W. Song, T. W. de Haas, H. Fadaei and D. Sinton, *Lab on a chip*, 2014, **14**, 4382-4390.
59. N. K. Karadimitriou, V. Joekar-Niasar, S. M. Hassanizadeh, P. J. Kleingeld and L. J. Pyrak-Nolte, *Lab on a chip*, 2012, **12**, 3413-3418.
60. R. M. Tiggelaar, F. Benito-Lopez, D. C. Hermes, H. Rathgen, R. J. M. Egberink, F. G. Mugele, D. N. Reinhoudt, A. van den Berg, W. Verboom and H. J. G. E. Gardeniers, *Chemical Engineering Journal*, 2007, **131**, 163-170.
61. N. S. K. Gunda, B. Bera, N. K. Karadimitriou, S. K. Mitra and S. M. Hassanizadeh, *Lab on a Chip*, 2011, **11**, 3785-3792.
62. B. Bera, S. K. Mitra and D. Vick, *Micron* 2011, **42**, 412-418.
63. S. Peng, Q. Hu, S. Dultz and M. Zhang, *Journal of Hydrology*, 2012, **472-473**, 254-261.
64. E. S. Amirtharaj, M. a. Ioannidis, B. Parker and C. D. Tsakiroglou, *Transport in Porous Media*, 2011, **86**, 135-154.
65. R. Pini, S. C. M. Krevor and S. M. Benson, *Advances in Water Resources*, 2012, **38**, 48-59.
66. J. Joseph, N. S. K. Gunda and S. K. Mitra, *Chemical Engineering Science*, 2013, **99**, 274-283.
67. N. K. Karadimitriou and S. M. Hassanizadeh, *Vadose Zone Journal*, 2012, **11**.
68. A. Rufai and J. Crawshaw, *Physics of Fluids*, 2017, **29**.
69. M. Buchgraber, M. Al-Dossary, C. M. Ross and A. R. Kovscek, *Journal of Petroleum Science and Engineering*, 2012, **86-87**, 27-38.
70. V. Er, T. Babadagli and Z. Xu, *Energy and Fuels*, 2010, **24**, 1421-1430.
71. K. Xu, T. Liang, P. Zhu, P. Qi, J. Lu, C. Huh and M. Balhoff, *Lab on a chip*, 2017, **17**, 640-646.
72. D. Crandall, G. Ahmadi, D. Leonard, M. Ferer and D. H. Smith, *The Review of scientific instruments*, 2008, **79**.
73. C. W. Hull, *United State Patent*, 1986, **Patent Number : 4575330**.
74. D. S. Park, J. Upadhyay, V. Singh, K. E. Thompson and D. E. Nikitopoulos, *Proceedings of the ASME 2015 International Mechanical Engineering Congress and Exposition.*, 2015, **10**.
75. W. Yun, C. M. Ross, S. Roman and A. R. Kovscek, *Lab on a chip*, 2017.
76. Y. Cinar, N. South, A. Riaz and H. A. Tchelepi, *SPE Journal*, 2009, **14**, 588-594.
77. A. M. Tartakovsky, G. Redden, P. C. Lichtner, T. D. Scheibe and P. Meakin, *Water Resources Research*, 2008, **44**.
78. A. T. Krummel, S. S. Datta, S. Münster and D. A. Weitz, *AIChE Journal*, 2013, **59**, 1022-1029.
79. S. A. Bowden, Y. Tanino, B. Akamairo and M. Christensen, *Lab on a Chip*, 2016, **16**, 4677-4681.
80. Y. Tanino, X. Zacarias-Hernandez and M. Christensen, *Experiments in Fluids*, 2018, **59**, 35.
81. C. Hu, J. E. Morris and R. L. Hartman, *Lab on a Chip*, 2014, **14**, 2014-2022.
82. S. Iglauer, *Accounts of Chemical Research*, 2017, **50**, 1134-1142.
83. B. Zhao, C. W. MacMinn and R. Juanes, *Proceedings of the National Academy of Sciences*, 2016, **113**, 10251-10256.
84. J. Botto, S. J. Fuchs, B. W. Fouke, A. F. Clarens, J. T. Freiburg, P. M. Berger and C. J. Werth, *Energy & Fuels*, 2017, **31**, 5275-5285.
85. D. Appelhans, D. Ferse, H. J. P. Adler, W. Plieth, A. Fikus, K. Grundke, F. J. Schmitt, T. Bayer and B. Adolphi, *Colloids & Surface A: Physicochemical and Engineering Aspects*, 2000, **161**, 203-212.
86. R. Hu, J. Wan, Y. Kim and T. K. Tokunaga, *International Journal of Greenhouse Gas Control*, 2017, **60**, 129-139.
87. R. Hu, J. Wan and T. K. Tokunaga, *Water Resources Research*, 2017, **53**, 6377-6394.
88. C. Chalbaud, M. Robin, J. Lombard, H. Bertin and P. Egermann, *Oil & Gas Science and Technology – Rev. IFP*, 2010, **65**, 541-555.
89. H. Lee, S. G. Lee and P. S. Doyle, *Lab On A chip*, 2015, **15**, 3047-3055.
90. W. Song and A. R. Kovscek, *Lab on a chip*, 2015, **15**, 3314-3325.
91. W. Song and A. R. Kovscek, *Journal of Natural Gas Science and Engineering*, 2016, **34**, 1276-1283.
92. T. Tosco, A. Tiraferri and R. Sethi, *Environmental Science & Technology*, 2009, **43**, 4425-4431.
93. G.-Q. Tang and N. R. Morrow, *Journal of Petroleum Science and Engineering*, 1999, **24**, 99-111.
94. Y. Q. Zhang, A. Sanati-Nezhad and S. H. Hejazi, *Lab on a Chip*, 2018, **18**, 285-295.
95. S. G. Lee, H. Lee, A. Gupta, S. Chang and P. S. Doyle, *Advanced Functional Materials*, 2016, **26**, 4896-4905.
96. W. Wang, S. Chang and A. Gizzatov, *ACS Applied Materials & Interfaces*, 2017, **9**, 29380-29386.
97. R. Singh, M. Sivaguru, G. A. Fried, B. W. Fouke, R. A. Sanford, M. Carrera and C. J. Werth, *Journal of Contaminant Hydrology*, 2017, **204**, 28-39.
98. B. A. Rizkin, F. G. Popovic and R. L. Hartman, *Journal of Vacuum Science & Technology A: Vacuum, Surfaces, and Films*, 2019, **37**, 050801.
99. T. Gavoille, N. Pannacci, G. Bergeot, C. Marliere and S. Marre, *Reaction Chemistry & Engineering*, 2019, **4**, 1721-1739.
100. C. Chang, Q. Zhou, T. J. Kneafsey, M. Oostrom, T. W. Wietsma and Q. Yu, *Advances in Water Resources*, 2016, **92**, 142-158.
101. G. Park, S.-O. Kim, M. Lee and S. Wang, *Energy Procedia*, 2017, **125**, 520-526.
102. C. Zhang, K. Dehoff, N. Hess, M. Oostrom, T. W. Wietsma, A. J. Valocchi, B. W. Fouke and C. J. Werth, *Environmental Science and Technology*, 2010, **44**, 7833-7838.
103. R. Biswas, J. E. Lewis and M. Maroncelli, *Chemical Physics Letters*, 1999, **310**, 485-494.
104. J. W. Grate, M. G. Warner, J. W. Pittman, K. J. Dehoff, T. W. Wietsma, C. Zhang and M. Oostrom, *Water Resources Research*, 2013, **49**, 4724-4729.
105. M. M. Martin and L. Lindqvist, *Journal of Luminescence*, 1975, **10**, 381-390.
106. K. Takehara and G. T. Etoh, *Gas Transfer at Water Surfaces*, 2013, **127**, 89-95.
107. Y. Senga, I. Tsutsui, K. Mishima, Y. Kakinuma and Y. Sato, *Proceedings PowerMEMS 2008*, 2008, 429-432.
108. J. G. Santiago, S. T. Wereley, C. D. Meinhart, D. J. Beebe and R. J. Adrian, *Experiments in Fluids*, 1998, **25**, 316-319.
109. J. Paiola, H. Auradou and H. Bodiguel, *Lab on a Chip*, 2016, **16**, 2851-2859.

110. C. D. Meinhart, S. T. Wereley and M. H. B. Gray, *Meas. Sci. Technol.*, 2000, **11**, 809-814.
111. F. Kazemifar, G. Blois, D. C. Kyritsis and K. T. Christensen, *Advances in Water Resources*, 2016, **95**, 352-368.
112. A. Perro, G. Lebourdon, S. Henry, S. Lecomte, L. Servant and S. Marre, *Reaction Chemistry & Engineering*, 2016, **1**, 577-594.
113. D. Li and Z. Duan, *Chemical Geology*, 2007, **244**, 730-751.
114. K. J. Kingma and R. J. Hemley, *American Mineralogist*, 1994, **79**, 269-273.
115. J. J. Freeman, A. Wang, K. E. Kuebler, B. L. Jolliff and L. A. Haskin, *The Canadian Mineralogist*, 2008, **46**, 1477-1500.
116. R. Singh, H. Yoon, R. A. Sanford, L. Katz, B. W. Fouke and C. J. Werth, *Environmental Science & Technology*, 2015, **49**, 12094-12104.
117. B. Pinho, K. Minsariya, A. Yen, N. Joshi and R. L. Hartman, *Energy & Fuels*, 2017, **31**, 11640-11650.
118. W. Chen, B. Pinho and R. L. Hartman, *Lab on a Chip*, 2017, **17**, 3051-3060.
119. J. Ari, G. Louvet, Y. Ledemi, F. Célarie, S. Morais, B. Bureau, S. Marre, V. Nazabal and Y. Messaddeq, *Science and Technology of Advanced Materials*, 2020, **21**, 11-24.
120. B. Lee, *Optical Fiber Technology*, 2003, **9**, 57-79.
121. R. Bogue, *Sensor Review*, 2011, **31**, 304-309.
122. B. Bao, L. Melo, B. Davies, H. Fadaei, D. Sinton and P. Wild, *Environmental Science and Technology*, 2013, **47**, 306-313.
123. F. Charpentier, B. Bureau, J. Troles, C. Boussard-Plédel, K. Michel-Le Pierrès, F. Smektala and J.-L. Adam, *Optical Materials*, 2009, **31**, 496-500.
124. F. Starecki, S. Morais, R. Chahal, C. Boussard-plédel, B. Bureau, F. Palencia, C. Lecoutre, Y. Garrabos, S. Marre and V. Nazabal, *International Journal of Greenhouse Gas Control*, 2016, **55**, 36-41.
125. T. Beuvier, E. A. C. Panduro, P. Kwaśniewski, S. Marre, C. Lecoutre, Y. Garrabos, C. Aymonier, B. Calvignac and A. Gibaud, *Lab on a chip*, 2015, **15**, 2002-2008.
126. Y. S. Oh, H. Y. Jo, J.-H. Ryu and G.-Y. Kim, *Journal of Hazardous Materials*, 2017, **324**, 373-381.
127. A. M. Alhammadi, A. Alratrout, K. Singh, B. Bijeljic and M. J. Blunt, *Scientific Reports*, 2017, **7**, 1-9.
128. L. Zuo, J. B. Ajo-Franklin, M. Voltolini, J. T. Geller and S. M. Benson, *Journal of Petroleum Science and Engineering*, 2017, **155**, 1-15.
129. J. M. Bray, E. G. Lauchnor, G. D. Redden, R. Gerlach, Y. Fujita, S. L. Codd and J. D. Seymour, *Environmental Science & Technology*, 2017, **51**, 1562-1569.
130. G. Mikolajczyk, L. Huang, M. Wilhelm, W. Dreher and S. Odenbach, *Chemical Engineering Science*, 2018, **175**, 257-266.
131. J. Bear, *Dynamics of fluids in porous media*, New York : Dover, 1988.
132. F. Dullien, *Porous Media : Fluid Transport and Pore Structure*, 1991.
133. Y. Zhao, Y. Song, Y. Liu, H. Liang and B. Dou, *Industrial & Engineering Chemistry Research*, 2011, **50**, 4707-4715.
134. J. C. Perrin and S. Benson, *Transport in Porous Media*, 2010, **82**, 93-109.
135. Y. Chen, D. Wu and R. Hu, *Water Resources Research*, 2017, **53**, 7756-7772.
136. R. T. Armstrong, N. Evseev, D. Koroteev and S. Berg, *Advances in Water Resources*, 2015, **77**, 57-68.
137. Y. Wang, N. Wei, C. Zhang, T. W. Wietsma, A. Bonneville, X. Li, M. Li and Z. Wang, *Microfluidics and Nanofluidics*, 2018, **22**, 101.
138. X. Zheng, N. Mahabadi, T. S. Yun and J. Jang, *Journal of Geophysical Research: Solid Earth*, 2017, **122**, 1634-1647.
139. S. Kim and J. C. Santamarina, *International Journal of Greenhouse Gas Control*, 2014, **20**, 324-332.
140. R. Holtzman and E. Segre, *Physical Review Letters*, 2015, **115**, 1-5.
141. H. S. Rabban, V. Joekar-niasar, T. Pak and N. Shokri, *Scientific Reports*, 2017, **7**.
142. S. Berg, S. Oedai and H. Ott, *International Journal of Greenhouse Gas Control*, 2013, **12**, 478-492.
143. M. Akbarabadi and M. Piri, *Advances in Water Resources*, 2013, **52**, 190-206.
144. P. Chiquet, D. F. Broseta and S. Thibeau, *SPE Europec/EAGE Annual Conference*, 2005, **SPE-94183-MS**.
145. S. Iglauder, C. H. Pentland and A. Busch, *Water Resources Research*, 2015, **51**, 729-774.
146. P. Chiquet, J.-L. Daridon, D. Broseta and S. Thibeau, *Energy Conversion and Management*, 2007, **48**, 736-744.
147. D. N. Espinoza and J. C. Santamarina, *Water Resources Research*, 2010, **46**.
148. C. Chen, Z. Chai, W. Shen, W. Li and Y. Song, *Energy & Fuels*, 2017, **31**, 7317-7324.
149. P. Fantinel, O. Borgman, R. Holtzman and L. Goehring, *Scientific Reports*, 2017, **7**.
150. P. Aussillous and D. Quéré, *Physics of Fluids*, 2000, **12**, 2367-2371.
151. J. Ennis-King and L. Paterson, *SPE Journal*, 2005, **10**.
152. S. E. Gasda, J. M. Nordbotten and M. A. Celia, *Water Resources Research*, 2011, **47**, 1-14.
153. C. W. MacMinn, M. L. Szulczewski and R. Juanes, *Journal of Fluid Mechanics*, 2010, **662**, 329-351.
154. C. W. MacMinn, M. L. Szulczewski and R. Juanes, *Energy Procedia*, 2011, **4**, 3904-3910.
155. E. Agartan, L. Trevisan, A. Cihan, J. Birkholzer, Q. Zhou and T. H. Illangasekare, *Water Resources Research*, 2015, **51**, 1635-1648.
156. T. J. Kneafsey and K. Pruess, *Transport in Porous Media*, 2010, **82**, 123-139.
157. N. Spycher, K. Pruess and J. Ennis-King, *Geochimica et Cosmochimica Acta*, 2003, **67**, 3015-3031.
158. Q. Zhou, Birkholzer JT, Mehnert E, Lin YF and Z. K., *Ground Water*, 2010, **48**, 494-514.
159. Q. Zhou, C. F. Tsang, J. Birkholzer and J. Rutqvist, *International Journal of Greenhouse Gas Control*, 2008, **2**, 626-639.
160. C. Chang, Q. Zhou, L. Xia, X. Li and Q. Yu, *International Journal of Greenhouse Gas Control*, 2013, **14**, 1-14.
161. C. Chang, Q. Zhou, J. Guo and Q. Yu, *International Journal of Greenhouse Gas Control*, 2014, **28**, 328-342.
162. L. Paterson, C. Boreham, M. Bunch, T. Dance, J. Ennis-King, B. Freifeld, R. Haese, C. Jenkins, T. LaForce, M. Raab, R. Singh, L. Stalker and Y. Zhang, *Energy Procedia*, 2013, **37**, 6140-6148.
163. W. J. Thomas and M. J. Adams, *Transactions of the Faraday Society*, 1965, **61**, 668-673.
164. A. Tamimi, E. B. Rinker and O. C. Sandall, *Journal of Chemical & Engineering Data*, 1994, **39**, 330-332.
165. S. Takenouchi and G. C. Kennedy, *American Journal of Science*, 1965, **263**, 445-454.

166. Y.-B. Chang, B. K. Coats and J. S. Nolen, *SPE Reservoir Evaluation & Engineering*, 1998, **1**, 155-160.
167. T. A. Renner, *SPE Reservoir Engineering*, 1988, **3**.
168. L. S. Wang and T. M. Guo, *Fluid Phase Equilibria*, 1996, **117**, 364-372.
169. M. M. Bahar and K. Liu, *SPE Asia Pacific Oil and Gas Conference and Exhibition*, 2008, **SPE-116513-MS**.
170. A. Sell, H. Fadaei, M. Kim and D. Sinton, *Environmental science & technology*, 2013, **47**, 71-78.
171. S. Hirai, K. Okazaki, H. Yazawa, H. Ito, Y. Tabe and K. Hijikata, *Energy*, 1997, **22**, 363-367.
172. E. Tumarkin, Z. Nie, J. I. Park, M. Abolhasani, J. Greener, B. Sherwood-Lollar, A. Günther and E. Kumacheva, *Lab on a chip*, 2011, **11**, 3545-3550.
173. Y. K. Kharaka, D. R. Cole, S. D. Hovorka, W. D. Gunter, K. G. Knauss and B. M. Freifeld, *Geology*, 2006, **34**, 577-580.
174. M. Abolhasani, M. Singh, E. Kumacheva and A. Günther, *Lab on a Chip*, 2012, **12**, 1611-1618.
175. T. Cubaud, M. Sauzade and R. Sun, *Biomicrofluidics*, 2012, **6**, 22002-220029.
176. C. Chang, Q. Zhou, T. J. Kneafsey, M. Oostrom and Y. Ju, *Advances in Water Resources*, 2019, **123**, 54-69.
177. S. Seo, M. Nguyen, M. Mastiani, G. Navarrete and M. Kim, *Analytical Chemistry*, 2017, **89**, 10827-10833.
178. L. Zuo and S. M. Benson, *Energy Procedia*, 2013, **37**, 6957-6963.
179. R. Li, P. Jiang, D. He, X. Chen and R. Xu, *Environmental Science & Technology*, 2017, **51**, 8869-8876.
180. R. Xu, R. Li, J. Ma, D. He and P. Jiang, *Accounts of Chemical Research*, 2017, **50**, 2056-2066.
181. L. Zuo, S. Krevor, R. W. Falta and S. M. Benson, *Transport in Porous Media*, 2012, **91**, 459-478.
182. R. Xu, R. Li, F. Huang and P. Jiang, *Science Bulletin*, 2017, **62**, 795-803.
183. J. E. Elkhoury, P. Ameli and R. L. Detwiler, *International Journal of Greenhouse Gas Control*, 2013, **16**, S203-S215.
184. N. Arsalan, J. J. Buiting and Q. P. Nguyen, *Colloids and Surfaces A: Physicochemical and Engineering Aspects*, 2015, **467**, 107-112.
185. P. Nguyen, H. Fadaei and D. Sinton, *Journal of Fluids Engineering*, 2013, **135**, 21203.
186. M. J. Bickle, *Nature Geoscience*, 2009, **2**, 815-818.
187. S. Bachu and J. J. Adams, *Energy Conversion and Management*, 2003, **44**, 3151-3175.
188. W. D. Gunter, S. Bachu and S. Benson, *Geological Society, London, Special Publications*, 2004, **233**, 129-145.
189. J. M. Matter and P. B. Kelemen, *Nature Geoscience*, 2009, **2**, 837-841.
190. R. Miri and H. Hellevang, *International Journal of Greenhouse Gas Control*, 2016, **51**, 136-147.
191. S. Sarig and F. Tartakovsky, *Journal of Crystal Growth*, 1975, **28**, 300-305.
192. C. Carteret, A. Dandeu, S. Moussaoui, H. Muhr, B. Humbert and E. Plasari, *Crystal Growth & Design*, 2009, **9**, 807-812.
193. R. J. Rosenbauer, T. Koksalan and J. L. Palandri, *Fuel Processing Technology*, 2005, **86**, 1581-1597.
194. L. Luquot and P. Gouze, *Chemical Geology*, 2009, **265**, 148-159.
195. E. Liteanu and C. J. Spiers, *Chemical Geology*, 2009, **265**, 134-147.
196. A. Lassin, L. André, N. Devau, A. Lach, T. Beuvier, A. Gibaud, S. Gaboreau and M. Azaroual, *Geochimica et Cosmochimica Acta*, 2018, **240**, 236-254.
197. G. E. Katz, B. Berkowitz, A. Guadagnini and M. W. Saaltink, *Journal of Contaminant Hydrology*, 2011, **120-121**, 27-44.
198. K. J. Davis, P. M. Dove and J. J. De Yoreo, *Science*, 2000, **290**, 1134-1137.
199. L. C. Nielsen, J. J. De Yoreo and D. J. DePaolo, *Geochimica et Cosmochimica Acta*, 2013, **115**, 100-114.
200. L. Fernandez-Diaz, A. Putnis, M. Prieto and C. V. Putnis, *Journal of Sedimentary Research*, 1996, **66**, 482-491.
201. S. Jaho, G. D. Athanasakou, V. Sygouni, M. G. Lioliou, P. G. Koutsoukos and C. A. Paraskeva, *Crystal Growth & Design*, 2016, **16**, 359-370.
202. R. Zhao and J. Cheng, *Greenhouse Gases: Science and Technology*, 2017, **7**, 624-636.
203. M. Nooraiepour, H. Fazeli, R. Miri and H. Hellevang, *Environmental science & technology*, 2018, **52**, 6050-6060.
204. S. C. Cao, J. Jung and M. Radonjic, *Microsystem Technologies*, 2019, **25**, 4035-4052.
205. J. Poonoosamy, C. Westerwalbesloh, G. Deissmann, M. Mahrous, E. Curti, S. V. Churakov, M. Klinkenberg, D. Kohlheyer, E. von Lieres and D. Bosbach, *Chemical Geology*, 2019, **528**, 119264.
206. C. Soulaine, S. Roman, A. Kovscek and H. A. Tchelepi, *Journal of Fluid Mechanics*, 2017, **827**, 457-483.
207. C. Soulaine, S. Roman, A. Kovscek and H. A. Tchelepi, *Journal of Fluid Mechanics*, 2018, **855**, 616-645.
208. C. Magnabosco, L.-H. Lin, H. Dong, M. Bomberg, W. Ghiorse, H. Stan-Lotter, K. Pedersen, T. Kieft, E. Van Heerden and T. C. Onstott, *Nature Geoscience*, 2018, **11**, 707-717.
209. W. B. Whitman, D. C. Coleman and W. J. Wiebe, *Proceedings of the National Academy of Sciences*, 1998, **95**, 6578-6583.
210. S. McMahon and J. Parnell, *FEMS Microbiology Ecology*, 2014, **87**, 113-120.
211. Y. M. Bar-On, R. Phillips and R. Milo, *Proceedings of the National Academy of Sciences*, 2018, **115**, 6506-6511.
212. A. Soudmand-asli, S. S. Ayatollahi, H. Mohabatkar, M. Zareie and S. F. Shariatpanahi, *Journal of Petroleum Science and Engineering*, 2007, **58**, 161-172.
213. M. S. Afrapoli, S. Alipour and O. Torsaeter, *Transport in Porous Media*, 2012, **93**, 705-719.
214. R. E. Lappan and H. S. Fogler, *Biotechnology and bioengineering*, 1996, **50**, 6-15.
215. D. Kim and H. S. Fogler, *Biotechnology and bioengineering*, 2000, **69**, 47-56.
216. N. Liu, T. Skauge, D. Landa-Marbán, B. Hovland, B. Thorbjørnsen, F. A. Radu, B. F. Vik, T. Baumann and G. Bødtker, *Journal of Industrial Microbiology & Biotechnology*, 2019, **46**, 855-868.
217. S. Dupraz, B. Ménez, P. Gouze, R. Leprovost, P. Bénézeth, O. S. Pokrovsky and F. Guyot, *Chemical Geology*, 2009, **265**, 54-62.
218. A. C. Mitchell, K. Dideriksen, L. H. Spangler, A. B. Cunningham and R. Gerlach, *Environmental Science & Technology*, 2010, **44**, 5270-5276.
219. Y. Fujita, J. L. Taylor, T. L. T. Gresham, M. E. Delwiche, F. S. Colwell, T. L. McLing, L. M. Petzke and R. W. Smith, *Environmental Science & Technology*, 2008, **42**, 3025-3032.

220. M. Zettlitzer, F. Moeller, D. Morozova, P. Lokay, H. Würdemann and C. S. Group, *International Journal of Greenhouse Gas Control*, 2010, **4**, 952-959.
221. J. Zhang, T. A. Davis, M. A. Matthews, M. J. Drews, M. LaBerge and Y. H. An, *Journal of Supercritical Fluids*, 2006, **38**, 354-372.
222. L. Zheng, J. A. Apps, Y. Zhang, T. Xu and J. T. Birkholzer, *Chemical Geology*, 2009, **268**, 281-297.
223. A. G. Carroll, R. Przeslawski, L. C. Radke, J. R. Black, K. Picard, J. W. Moreau, R. R. Haese and S. Nichol, *Continental Shelf Research*, 2013, **83**, 116-128.
224. G. Bertoloni, A. Bertucco, V. De Cian and T. Parton, *Biotechnology and Bioengineering*, 2006, **95**, 155-160.
225. M. K. Oulé, K. Tano, A.-M. Bernier and J. Arul, *Canadian journal of microbiology*, 2006, **52**, 1208-1217.
226. A. C. Mitchell, A. J. Phillips, R. Hiebert, R. Gerlach, L. H. Spangler and A. B. Cunningham, *International Journal of Greenhouse Gas Control*, 2009, **3**, 90-99.
227. M. Thullner, J. Zeyer and W. Kinzelbach, *Transport in Porous Media*, 2002, **49**, 99-122.
228. D. A. Glatstein and F. M. Francisca, *Environmental Technology*, 2014, **35**, 1886-1892.
229. V. Sygouni, I. D. Manariotis and C. V. Chrysikopoulos, *International Journal of Greenhouse Gas Control*, 2016, **46**, 240-247.
230. I. A. Vasiliadou and C. V. Chrysikopoulos, *Water Resources Research*, 2011, **47**, 1-14.
231. S. Dupraz, M. Parmentier, B. Ménez and F. Guyot, *Chemical Geology*, 2009, **265**, 44-53.
232. A. C. Mitchell, A. Phillips, L. Schultz, S. Parks, L. Spangler, A. B. Cunningham and R. Gerlach, *International Journal of Greenhouse Gas Control*, 2013, **15**, 86-96.
233. A. J. Phillips, E. Lauchnor, J. J. Eldring, R. Esposito, A. C. Mitchell, R. Gerlach, A. B. Cunningham and L. H. Spangler, *Environmental Science & Technology*, 2013, **47**, 142-149.
234. N. Youssef, M. S. Elshahed and M. J. McInerney, *Advances in applied microbiology*, 2009, **66**, 141-251.
235. V. A. Lifton, *Lab on a Chip*, 2016, **16**, 1777-1796.
236. K. He, L. Xu, Y. Gao, X. Yin and K. B. Neeves, *Journal of Petroleum Science and Engineering*, 2015, **135**, 531-541.
237. P. Nguyen, PhD Thesis, University of Toronto (Canada), 2016.
238. Z. Song, W. Zhu, X. Wang and S. Guo, *Energy & Fuels*, 2018, **32**, 3194-3201.
239. A. Sharbatian, A. Abedini, Z. Qi and D. Sinton, *Analytical Chemistry*, 2018, **90**, 2461-2467.
240. J. Vilcáez, L. Li, D. Wu and S. S. Hubbard, *Geomicrobiology Journal*, 2013, **30**, 813-828.
241. M. S. Karambeigi, M. Schaffie and M. H. Fazaelipoor, *Petroleum Science and Technology*, 2013, **31**, 923-931.
242. L. R. Brown, *Current Opinion in Microbiology*, 2010, **13**, 316-320.
243. R. Sen, *Progress in energy and combustion Science*, 2008, **34**, 714-724.
244. M. Safdel, M. A. Anbaz, A. Daryasafar and M. Jamialahmadi, *Renewable and Sustainable Energy Reviews*, 2017, **74**, 159-172.
245. H. Amani, *Journal of Petroleum Science and Engineering*, 2015, **128**, 212-219.
246. R. T. Armstrong and D. Wildenschild, *Journal of Petroleum Science and Engineering*, 2012, **94-95**, 155-164.
247. A. Picard and I. Daniel, *Biophysical chemistry*, 2013, **183**, 30-41.
248. A. Cario, G. C. Oliver and K. L. Rogers, *Frontiers in Earth Science*, 2019, **7**, 225.
249. M. Ranchou-Peyruse, J.-C. Auguet, C. Mazière, C. X. Restrepo-Ortiz, M. Guignard, D. Dequidt, P. Chiquet, P. Cézac and A. Ranchou-Peyruse, *Environmental Microbiology*, 2019, **21**, 3953-3964.
250. T. R. Ginn, B. D. Wood, K. E. Nelson, T. D. Scheibe, E. M. Murphy and T. P. Clement, *Advances in Water Resources*, 2002, **25**, 1017-1042.
251. J. Vilcáez, *Journal of Petroleum Science and Engineering*, 2015, **135**, 583-595.
252. T. Park, H.-W. Joo, G.-Y. Kim, S. Kim, S. Yoon and T.-H. Kwon, *Frontiers in Microbiology*, 2017, **8**.
253. J. Zhong, A. Abedini, L. Xu, Y. Xu, Z. Qi, F. Mostowfi and D. Sinton, *Nanoscale*, 2018, **10**, 21994-22002.
254. Y. Zhao, Y. Wang, J. Zhong, Y. Xu, D. Sinton and Z. Jin, *Langmuir*, 2018, **34**, 14058-14068.
255. J. Zhong, Y. Zhao, C. Lu, Y. Xu, Z. Jin, F. Mostowfi and D. Sinton, *Langmuir*, 2018, **34**, 9927-9935.
256. A. Jatukaran, J. Zhong, A. H. Persad, Y. Xu, F. Mostowfi and D. Sinton, *ACS Applied Nano Materials*, 2018, **1**, 1332-1338.
257. A. A. Hasham, A. Abedini, A. Jatukaran, A. Persad and D. Sinton, *Journal of Petroleum Science and Engineering*, 2018, **165**, 181-186.